LATVIAN JOURNAL of PHYSICS and TECHNICAL SCIENCES

ISSN 0868 - 8257

(Vol. 54)

2017

Ind. pasūt. € 1,50 Indekss 2091
Org. € 15,00 Indekss 2092

SATURS

ENERĢĒTIKAS FIZIKĀLĀS UN TEHNISKĀS PROBLĒMAS

LIETIŠĶĀ FIZIKA

ELEKTRONIKA

Price to individual subscribers € 1.50/issue Index 2091
Price to collective subscribers € 15.00/issue Index 2092

CONTENTS

PHYSICAL AND TECHNICAL ENERGY PROBLEMS

APPLIED PHYSICS

ELECTRONICS

Индивид. заказ. € 1,50 Индекс 2091
Орг. заказ. € 15,00 Индекс 2092

СОДЕРЖАНИЕ

LATVIAN JOURNAL of PHYSICS and TECHNICAL SCIENCES

LATVIJAS FIZIKAS un TEHNISKO ZINĀTŅU ŽURNĀLS

ЛАТВИЙСКИЙ ФИЗИКО-ТЕХНИЧЕСКИЙ ЖУРНАЛ

Published six times a year since February 1964
Iznāk sešas reizes gadā kopš 1964. gada februāra
Выходит шесть раз в год с февраля 1964 года

6 (Vol. 54) • 2017

RĪGA

INDEKSĒTS (PUBLICĒTS) | INDEXED (PUBLISHED) IN

www.scopus.com
www.degruyter.com
EBSCO (Academic Search Complete, www.epnet.com), INSPEC (www.iee.org.com). VINITI (www.viniti.ru), Begell House Inc/ (EDC, www.edata-center.com).

Izdevējs: Fizikālās enerģētikas institūts
Reģistrācijas apliecība Nr. 0221
Redakcija: Krīvu iela 11, Rīga, LV-1006
Tel. 67551732, 67558694
e-pasts: ezerniec@edi.lv
Interneta adrese: www.fei-web.lv
Iespiests SIA “AstroPrint”

LATVIAN JOURNAL OF PHYSICS AND TECHNICAL SCIENCES
2017, N 6

DOI: 10.1515/lpts-2017-0036

PHYSICAL AND TECHNICAL ENERGY PROBLEMS

DEVELOPMENT AND COMPARISON OF TECHNICAL SOLUTIONS FOR ELECTRICITY MONITORING EQUIPMENT

A. Potapovs, A. Obushevs
Smart Grid Research Centre
Institute of Physical Energetics
11 Krivu Street, Riga, LV-1006, LATVIA

The paper focuses on the elaboration of a demand-side management platform for optimal energy management strategies; the topicality is related to the description and comparison of the developed electricity monitoring and control equipment. The article describes two versions based on Atmega328 and STM32 microcontrollers, a lower and higher level of precision, and other distinct performance parameters. At the end of the article, the results of the testing of the two types of equipment are given and their comparison is made.

Keywords: *demand side management, demand response, Internet of Things, monitoring, sockets, voltage measurement*

1. INTRODUCTION

The trend to strengthen consumers' flexibility in the e-market environment is conditioned by a wider expansion of Smart Grid Technologies, including Intelligent Metering Systems. Prospectively, bulk installations of Smart Meters alongside with the development of more flexible appliances should lead to the widespread public acceptance and deployment of price-responsive demand [1], [2].

To achieve a high level of reliability and robustness in power systems, the grid is designed for peak demand rather than the average load. This can result in under-utilised power generation and distribution systems and a waste of natural resources. Moreover, most of the fast responding generators that are used to meet the peak load, such as gas and coal units, are expensive and have large carbon footprints. To overcome these problems, different programs have been proposed to shape users' energy consumption profiles. Such programs allow the available generation capacity to be employed more efficiently so that a new generation and transmission infrastructure does not have to be installed. These programs, generally known as demand-side management (DSM), aim either at reducing consumption or shifting consumption.

Most of the current load control decisions in existing DSM systems are made manually, which makes it difficult for the participants to monitor the real-time prices

and use other advanced pricing methods. In fact, a lack of knowledge among end users about how to respond to time-varying prices is currently the main barrier for fully utilising the benefits of real-time pricing methods and DSM, in general. This problem can be resolved by equipping users with home automation systems and by implementing automated energy consumption scheduling units that can draw on pricing information to schedule the operation of various residential appliances on behalf of customers [3].

The present research aims to compare two different schematic solutions for power monitoring and control equipment in order to choose the most efficient one by comparing parameters such as electricity consumption, current and voltage measurement accuracy, samples per second, price and potential for future improvements.

2. HOME AREA NETWORK MONITORING & CONTROL

The Demand Side Management-Smart Home Lab of the Smart Grid Research Centre (presented in Fig. 1) is equipped with the developed monitoring & control socket hardware (Fig. 2) for the elaboration of a DSM platform based on the open source solution proposed in the OpenEnergyMonitor project [4] with the following features: sending data at periodic intervals to a web-connected base-station; real-time monitoring of active, reactive, apparent powers, currents, voltage and extra sensors (temperature, humidity, etc.); remote control possibility (switch off/on socket devices); easily customised for a variety of applications.

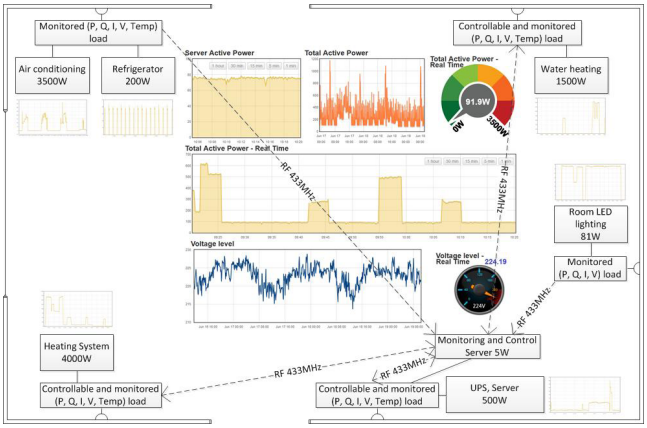

Fig. 1. Home area network facility with real-time monitoring & control.

3. MONITORING & CONTROL HARDWARE DESIGN

A. First Version of Real-Time Energy Monitoring and Control System

The first version of the device, described in more detail in [4], [5], operates on the basis of 8-bit Atmega 328 microcontroller (Fig. 2). A network transformer with two secondary windings is used to power the plates and measure network voltages, while the current transformer is used to measure the load current. An electromag-

netic relay is used to control the load. To transmit data using the radio network, the radio module RFM12B is used, operating in the 433 MHz band.

On the basis of the experimental operation of the device, the following characteristic shortcomings have been discovered in the device scheme:

a. Analogue signals are read out using the 10-bit ADC built-in Atmega328 microcontroller, which allows reading network voltage/current with $3.22 \cdot 10^{-3} V$ step, automatically providing low voltage and current measurement accuracy;
b. Under actual operating conditions, the performance of Atmega 328 microcontroller ADC is also characterised by a low sampling frequency equal to 35kSPS (samples per second) in case of using one ADC and 7.5kSPS using two ADC conversions, which makes it difficult to accurately detect zero point, and also reduces the accuracy of current and voltage measurement at various pulsed loads;
c. A network voltage transformer is used to read the network voltage, which is characterised by a specific nonlinearity, and its secondary winding voltage changes its value depending on the total load of the transformer (the relay operates or not, the radio is transmitting or not, etc.);
d. The design is not compact enough to be used comfortably as a smart socket.

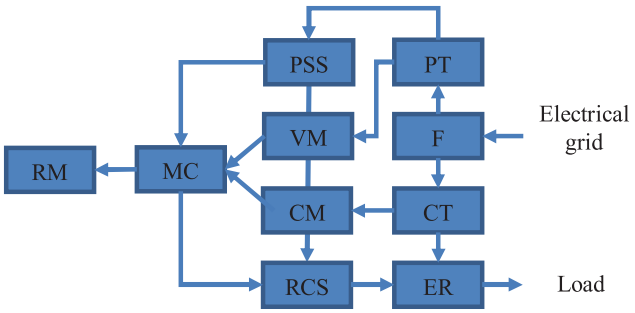

Fig. 2. Old version of socket monitoring & control hardware.

The first version of the device contains the following components: MC – 8-bit microcontroller Atmega 328; PT – dual secondary winding power transformer 230V to 2 x 6V; CT – linear current transformer 1500:1, 15A; VMS – voltage meter scheme; CMS – current meter scheme; PSS – 3.3V power source scheme; RM – radio module RFM12B; RCS – relay control scheme; R – electromagnetic relay 230V, 16A; F – fuse 16A.

B. Second Version of Real-Time Energy Monitoring and Control System

After defining shortcomings of the first version, a new electricity monitoring and control scheme has been developed (Fig. 3). The new version of the device is based on the 32-bit microcontroller STM32. The current measurement is carried out using a current sensor, but the voltage measurement is performed without a galvanic reference using only the voltage divider and the midpoint of the artificial supply

voltage. For the provision of radio communications, the system contains the RFM-69HW radio module, which provides stable indoor communication with the central control point in the indoor environment, within meters and more. The load control board, like its first version, is equipped with a 16A electromagnetic relay. Component feed plate contains 3W AC-DC pulse power supply with 3.3V DC output voltage.

Analogue signals are read out using the 16 bit ADC built-in STM32 microcontroller, which allows reading network voltage/current with $5 \cdot 10^{-5} V$ step, automatically providing high voltage and current measurement accuracy. The performance of microcontroller ADC is also characterised by a high sampling frequency equal to 135kSPS for one ADC and 30kSPS for two ADC conversion, which makes it more accurately detect zero points, and also increase the accuracy of current and voltage measurement at various pulsed loads.

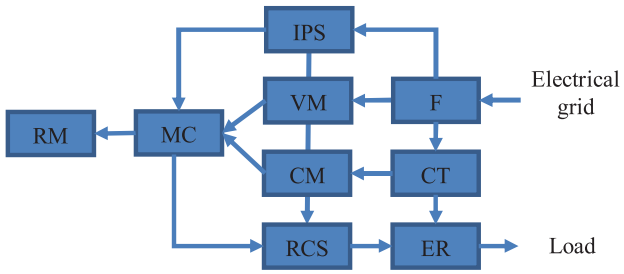

Fig. 3. New version of socket monitoring & control hardware.

The second version of the device contains the following components: MC – 32-bit microcontroller STM32; IPS – impulse power supply 230V to 3.3V; CT – linear current transformer 1500:1, 15A; VMS – voltage meter scheme; CMS – current meter scheme; RM – radio module RFM69HW; RCS – relay control scheme; R – electromagnetic relay 230V, 16A; F – fuse 16A, varistor 270V.

4. MATHEMATICAL MODEL OF ELECTRICAL PARAMETER MEASUREMENT

Root mean square (RMS) voltage and current values determine the operation of the electrical system (the electric heater generates heat in direct dependence on the RMS values of the voltage and current of the network). To sample a number of values over the network voltage period, it is necessary to sum the squares of the sample points, divide by the number of points per period (when determining the number of sample points, the Nyquist–Shannon sampling theorem is taken into account), and make the square root of the obtained result.

In a real network, at near zero voltage, there can be both “zero shelves” and repeated transitions through zero voltage, which will significantly introduce an error in the measurement. To overcome this issue, voltage tolerance zones are introduced (introducing the boundary of the zero-crossing voltage from the positive and negative sides), usually $0.05V$ in both directions, and also the frequency insensitivity zones (limiting the permissible frequency of the voltage signal).

Using the digitized data from the 16-bit ADC derived from delta-sigma on the built-in microcontroller, voltage and current root mean square values are calculated based on their average quadratic values during 10 periods.

5. RESULTS AND DISCUSSION

Preliminary test results with technology comparison are presented in Table 1 and Fig. 4, where second equipment generation demonstrates significant improvements in price, computation speed and memory.

Table 1

Comparison between the First and Second Versions

	I	**II**
	ATMEGA328	**STM32**
Flash, Kbytes	32	256
SRAM, Kbytes	2	32
CPU, MHz	20	72
ADC speed, kSPS	9.6–50	125–1000
Equipment consumption, W	0.83	0.42
SPS at 10 cycle period	5720	26800
MAE, V	0.1921	0.1455
RMSE, V	0.2458	0.1759
MAX Error, V	0.6415	0.4130
Price, EUR €	3.62	2.55

To compare voltage measurements, PMU (Phasor Measurement Unit) has been used and assumed as a voltage reference with high precision. Voltage errors are still significant from the voltage regulation point of view, and the primary field of precision improvement is the implementation of more advanced mathematical techniques such as FFT (Fast Fourier Transform) algorithms. However, from the perspective of energy regulation (demand response based on energy price signals), these errors are sufficient.

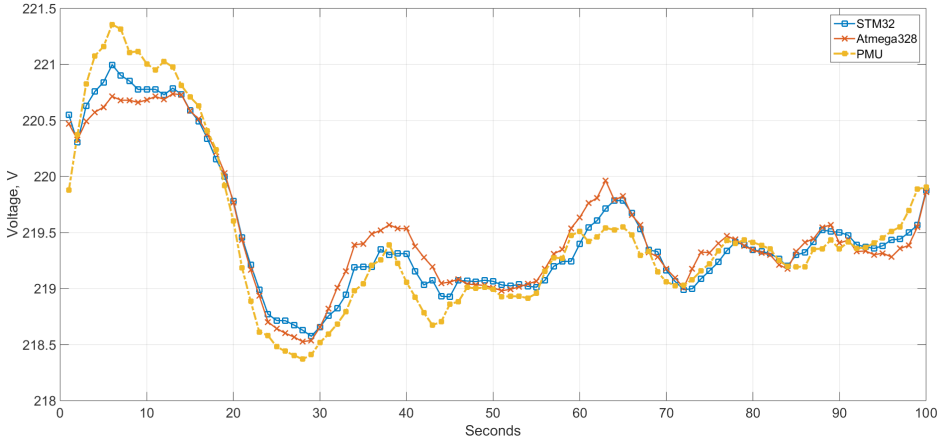

Fig. 4. Comparison between voltage measurements.

6. CONCLUSIONS AND FURTHER RESEARCH

A smart metering system has been developed to support the development of a new metering infrastructure, which could be the first step for network management system integration. The present research has been dedicated to the development and comparison of two inexpensive technical solutions (smart sockets) for electricity monitoring with sufficient precision and control possibilities. Experimental operation of the first device has demonstrated inherent shortcomings, which have been solved with a more advanced second generation device (faster, cheaper and precise).

Implementation of more advanced mathematics can provide accuracy improvement deriving parameters (V, I, P, Q) and bring an opportunity to obtain new observables such as frequency and harmonics.

ACKNOWLEDGEMENTS

The research has been supported by ERA-Net Smart Grids Plus project CLOUDGRID No. 77547 (Transnational CLOUD for Interconnection of Demonstration Facilities for Smart GRID Lab Research & Development), with support from the European Unions Horizon 2020 research and innovation programme.

REFERENCES

1. Turcik, M., Oleinikova, I., & Kolcun, M. (2011). *End-users' energy management strategies in market environment*. Presentation at the International Scientific Symposium Elektroenergetika, 21–23 September 2011, High Tatras, Slovakia.
2. Oleinikova, I., Mutule, A., Obushevs, A., & Antoskovs, N. (2016). Smart grid development: Multinational demo project analysis. *Latvian Journal of Physics and Technical Sciences*, *6*, ISSN 0868-8257 DOI: 10.1515/lpts-2016-0038
3. Samadi, P., Mohsenian-Rad, H., Wong, V. W. S., & Schober, R. (2015). The role of demand side management. *IEEE Smart Grid Newsletter Compendium*, 37–38.
4. Open Energy Monitor. (n.d.). Available at http://openenergymonitor.org/
5. Obushevs, A., Oleinikova, I., Mutule, A., & Potapovs, A. Demand side management platform for HAN flexibility estimation. In Proceedings of the 56th Annual International Scientific Conference of Riga Technical University, Section "Power and Electrical Engineering", 14 October 2015, Riga, Latvia. ISBN 978-1-4673-9752-0.

ELEKTROENERĢIJAS MONITORINGA IEKĀRTU TEHNISKO RISINĀJUMU IZSTRĀDE UN SALĪDZINĀJUMS

A.Potapovs, A. Obuševs

K o p s a v i l k u m s

Dotais raksts veltīts pieprasījuma vadības platformas izstrādei optimālās elektroenerģijas pārvaldības stratēģijai, pievēršot galveno uzmanību izstrādātās elektroenerģijas uzraudzības un kontroles iekārtu aprakstam un salīdzināšanā. Rakstā aprakstītas divas versijas, kuru pamatā ir Atmega328 un STM32 mikrokontrolleri ar augstāko un zemāko precizitāti, kā arī citi atšķirīgi veiktspējas parametri. Nobeigumā doti detalizēti abu piedāvājamo iekārtu testēšanas rezultāti, veikts to salīdzinājums, kā arī izteikti secinājumi par tiem.

03.11.2017.

LATVIAN JOURNAL OF PHYSICS AND TECHNICAL SCIENCES
2017, N 6

DOI: 10.1515/lpts-2017-0037

MODELLING THE SPATIAL DISTRIBUTION OF WIND ENERGY RESOURCES IN LATVIA

S. Aniskevich[1], V. Bezrukovs[2,3], U. Zandovskis[1], D. Bezrukovs[4]
[1]Latvian Environment, Geology and Meteorology Centre,
165 Maskavas Str., Riga, LV-1019, LATVIA
e-mail: svetlana.aniskevica@lvgmc.lv,
[2]Institute of Physical Energetics,
11 Krivu Str., Riga, LV-1006, LATVIA
[3]Ventspils University College,
101 Inzenieru Str., Ventspils, LV-3601, LATVIA
e-mail: elmag@inbox.lv,
[4]Riga Technical University
Arzenes Srt., 12/1, Riga, LV-1048, LATVIA

The paper studies spatial wind energy flow distribution in Latvia based on wind speed measurements carried out at an altitude of 10 *m* over a period of two years, from 2015 to 2016. The measurements, with 1 *min* increments, were carried out using certified measuring instruments installed at 22 observation stations of the Latvian National Hydrometeorological and Climatological Service of the Latvian Environment, Geology and Meteorology Centre (LEGMC). The models of the spatial distribution of averaged wind speed and wind energy density were developed using the method of spatial interpolation based on the historical measurement results and presented in the form of colour contour maps with a 1x1 *km* resolution. The paper also provides the results of wind speed spatial distribution modelling using a climatological reanalysis ERA5 at the altitudes of 10, 54, 100 and 136 *m* with a 31x31 *km* resolution. The analysis includes the comparison of actual wind speed measurement results with the outcomes of ERA5 modelling for meteorological observation stations in Ainazi, Daugavpils, Priekuli, Saldus and Ventspils.

Keywords*: wind speed, wind energy, measurements, modelling, ERA5.*

1. INTRODUCTION

The territory of Latvia does not possess any significant reserves of fossil fuels. Therefore, the needs of the national economy are mainly met through the import of electricity and energy carriers. This creates the dependency of the country's economy on external supplies. Hence, the state is interested in the development of power plants using available national energy resources [1].

The availability of financial support from the European Development Funds stimulates the construction of power generating stations [2]. This fact also encourages investors to consider the commercial use of alternative renewable energy sources, which are available for use on the industrial scale.

Favourable geographical location of the country on the shore of the Baltic Sea makes its territory open from the western direction for southwestern winds, which are prevailing in this region. The western part of Latvia is dominated by forest-covered plains, while in the eastern part of the country there are hilly areas of up to 300 *m* high.

Wind flows from the sea possess a significant wind energy potential, which can be used to produce electricity. Wind speed measurement results performed with 1 min increments allow us to calculate the density of wind energy that a wind current in a given region can carry. Based on the information, an estimate of the average annual power production for the projected Wind Power Plants (WPP) can be made [3], [4].

When choosing a construction site for a WPP, it is necessary to take into account the natural specificities of the landscape and estimate the density of wind energy in the given area. In this regard, information on the spatial distribution of the resource of wind energy on the entire territory of the country is of utmost importance for the national economy [5].

The rest of the paper is structured as follows: Section 2 provides the description of meteorological stations in Latvia and measuring equipment. Section 3 presents the model of spatial distribution of wind speed measurements obtained at the altitude of 10m. Section 4 introduces the model of spatial distribution of wind energy resources in Latvia. Section 5 presents summarised results, discusses their implications and makes conclusions.

2. THE NETWORK OF METEOROLOGICAL STATIONS AND MEASUREMENT RESULTS

In Latvia, for more than 100 years, there has been a network of meteorological observation stations that perform the collection and archiving of high quality representative meteorological data. For the measurements at the stations, only calibrated sensors and certified equipment, according to international requirements, are used. The monitoring of climate and weather conditions is carried out at 22 stations, shown in Fig. 1. A majority of the stations are currently operating in an automated mode.

The stations continuously measure and record the speed and direction of wind, measure atmospheric pressure, humidity and air temperature, as well as other meteorological parameters. In order to measure wind speed over the considered time period, 10 stations were equipped with Vaisala WAA 151 anemometers, while 8 stations had Vaisala WMT 702 ultrasonic wind sensors and at 4 stations anemometers were replaced by ultrasonic sensors.

In order to calculate the average wind speed with 1 *min* increments, an anemometer measures the actual wind speed every 2 *s*, while the ultrasonic sensor – every 3 *s*. All wind speed sensors are installed at a height of 10 *m*, except for Riga (36 *m*), Kolka (20 *m*) and Pavilosta (since December 2015 – 18 *m*) meteorological

observation stations. Prior to the analysis, outliers were removed from the dataset.

There are a number of publications devoted to the issue of estimating the magnitude of wind energy resource potential and its distribution on the territory of Latvia [6]–[9]. However, the reliability of these studies is not high, as they are based on the analysis of accessible public wind speed data, which is designed to study climate change. The correct estimates can be done only based on the analysis of the results of wind speed measurements performed simultaneously and at the same height above the ground in different regions of the country for a period of at least one year.

This article is based on data obtained using certified measuring sensors installed at meteorological observation stations belonging to the LEGMC[1]. The results of physical measurements are recorded as discrete values of wind speed with 1 *min* increments from 22 observation stations at 10 *m* height above the ground, over a period from 01/01/2015 to 31/12/2016.

Fig. 1. Map of Latvia with the locations of 22 meteorological stations and the mean elevation above sea level (*m)* with a 1x1 *km* resolution.

The presentation of the results of physical measurements in the form of a model of the spatial distribution of wind speed allows us to consider, as an alternative, other methods related to wind speed prediction. For instance, the article also presents the models of the spatial distribution of wind speed at the heights of 10, 54, 100 and 136 *m*, developed by using climatological reanalysis datasets ERA5 from 2015 to 2016 for the Latvian territory [10].

3. THE MODEL OF WIND SPEED SPATIAL DISTRIBUTION

The uniform distribution of observation stations on the territory of the country and a long measurement period allow us to present the results as a visual model in Fig. 2. The colour palette used in the model allows allocating areas in the territory

[1] https://www.meteo.lv/meteorologijas-operativa-informacija

of Latvia with the same level of wind speed. In this case, the spatial distribution of the average value of the wind speed V_{avg} is depicted in steps of 0.5 *m/s*. The value of the average wind speed for the measurement period at the measurement points was calculated as follows:

$$V_{avg} = \frac{1}{n}\sum_{i=1}^{n} V_i, \tag{1}$$

where V_i – the average wind speed with 1 *min* increments, *m/s*;

n – the number of measurements for the observation period from 01/01/2015 to 31/12/2016;

i – observation 1, 2, 3, …, n.

In order to estimate the value of the meteorological parameter between the observation stations, a spatial interpolation of measured data was used. In this article, a geostatistical method – universal kriging – was applied [11].

Apart from the observed values from the nearest stations, this method also uses additional spatial factors that influence meteorological parameters. The most relevant factors for average wind speed interpolation are geographical coordinates in the metric system LKS-92, elevation above the sea level and distance from the Baltic Sea or the Gulf of Riga. Spatial interpolation is performed on a grid with a resolution of 1x1 *km*.

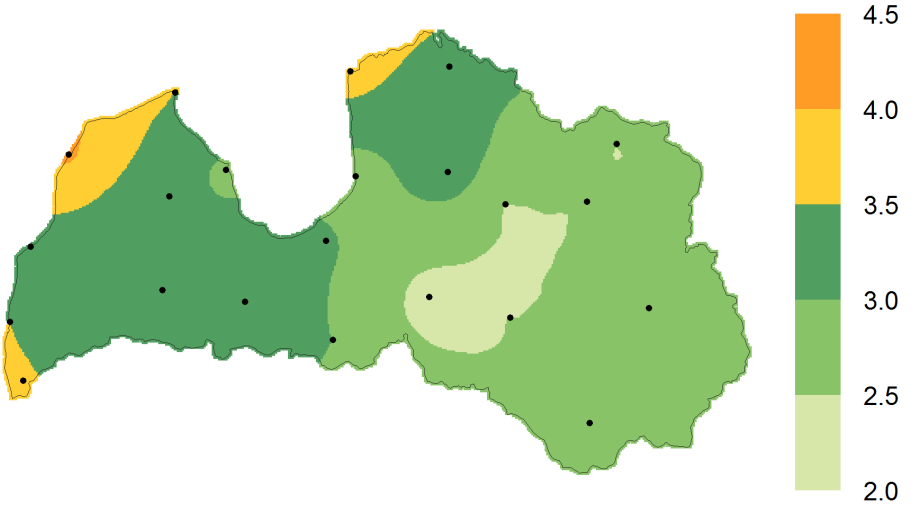

Fig. 2. Model of the spatial distribution of average values of wind speed *m/s* at an altitude of 10 *m* above the ground on the territory of Latvia.

Modern weather modelling technologies allow predicting the magnitude of wind speed above the surface of land and sea. For example, climatological reanalysis dataset ERA5, created by the European Centre for Medium-Range Weather Forecasts (ECMWF), provides information for a variety of meteorological parameters. ERA5 covers the Earth with a 31 *km* grid and stratifies the atmosphere into 137

levels from the surface up to the height of 80 *km*. The first 7-year segment of the ERA5 dataset is now available for public use [12]. The information available to users allows obtaining the average wind speed with 2 h increments for any point on the surface of the Earth. Figs. 3 and 4 present the models of spatial distribution of wind speeds in the territory of Latvia for the heights of 10, 54 *m* and 100, 136 *m*, respectively, which are estimated using the ERA5 dataset over a time period from 01/01/2015 to 31/12/2016.

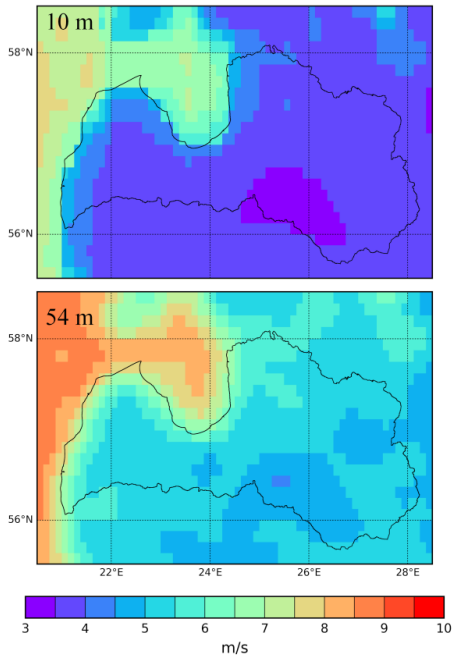

Fig. 3. Models of spatial distribution of average wind speed at the heights for 10 *m* and 54 *m*, estimated using ERA5.

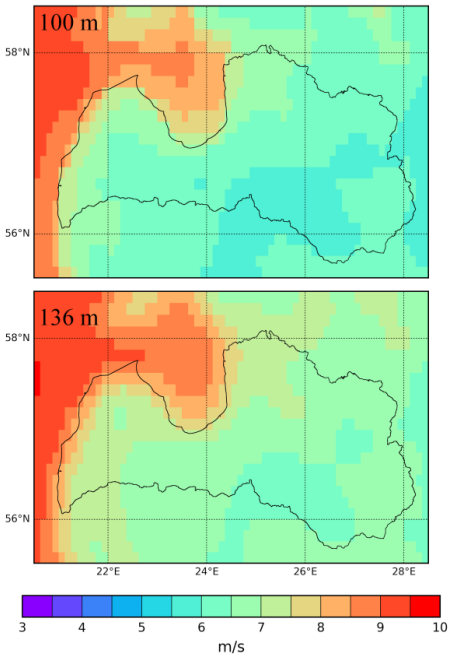

Fig. 4. Models of spatial distribution of average wind speed at the heights for 100 *m* and 136 *m*, estimated using ERA5.

The use of these models does not guarantee high accuracy and resolution, in contrast to physical measurements obtained at the observation stations, but it shows how the boundaries of the wind speed distribution regions change with an increasing altitude. The models also allow identifying the presence of areas that have relatively low and high potentials for wind energy. Specifically, wind speed on the coast of the Baltic Sea in the western part of the country is much higher than in the east, while the lowest values of wind speed are recorded in the central part of the country.

The results of wind speed measurements at meteorological observation stations in the area of Ainazi, Daugavpils, Priekuli, Saldus and Ventspils and ERA5 simulations are given in Table. Comparative analysis of these data shows that the results of ERA5 simulation consistently exceed the measured historical values in all regions by ~ (20–50) %. It is likely that ERA5 modelling results are strongly influenced by the structure of the terrain. However, modelling results presented in the form of contour maps can serve as a basis for estimating and comparing the intensity of wind speed in the central part of the country and on the shores of the Baltic Sea. That makes them useful at the planning stage – in the process of selecting the most

suitable sites for WPP construction and predicting the distribution of wind energy potential on the territory of Latvia.

In order to estimate the reliability of ERA5 simulation, the values of wind speed at the heights of 54, 100 and 136 *m* can be crosschecked with the results of physical measurements at the heights of up to 200 *m* above the ground in the time period from 01/03/2014 to 01/03/2015 obtained using laser measuring complex Pentalum SpiDAR [13]. Historical wind speed measurements used for the comparison were carried out in the coastal zone of Latvia – in Ventspils region. The performed comparison shows that the deviation of the results of physical wind speed measurements at the altitudes of 54, 100 and 136 *m* from the estimates of the average wind speed values obtained using ERA5 technology does not exceed 20 %. As the altitude above the ground level increases, the turbulence of airflows decreases; therefore, the use of simulation technology gives higher accuracy in determining wind speed.

An important observation with respect to the models of spatial distribution of wind speed at the heights of 54, 100 and 136 *m* is the continuous evolution of the boundary pattern, which determines the transition of the velocity levels. This indicates the preservation of the regularity of the change in the magnitude of the wind speed with increasing altitude.

4. MODEL OF THE SPATIAL DISTRIBUTION OF WIND ENERGY

The value of the energy unit density that a uniform airflow carries over an area of 1 m^2 is represented as follows:

$$P = \frac{1}{2}\rho V^3, \tag{2}$$

where ρ – is air density (*1.23 kg/m³* for a standard condition at the sea level and temperature *15° C)*;

V – is wind speed, *m/s* [14].

As follows from Eq. 2, the magnitude of the airflow energy is in a cubic relationship with its speed V. Therefore, in order to estimate wind energy, the magnitude of which is constantly changing, it is not correct to use the average wind speed calculated by Eq. 1. However, it should be noted that, in practice, wind speed values recorded in the database are discrete values, representing averaged results of measurements made over a certain time interval. When working with a large amount of data obtained over a long period of observations it is practical to split wind speed measurement results into bins that correspond to the speed intervals of a certain size. For each bin, the total recurrence time, expressed as a percentage of the total measurement time, is determined. The resulting frequency distribution function for the average wind speed characterises the qualitative side of the wind data and is used to estimate the energy carried by the flow with an uneven speed.

The curves depicted in Fig. 5 are functions of the empirical frequency distribution of bin values corresponding to the discrete measures of the average wind

speed V_{avg} with an interval of 1 *m/s*. The results of the measurements were obtained at meteorological observation stations in Ainazi, Daugavpils, Priekuli, Saldus and Ventspils during the measurement period from 01/01/2015 to 31/12/2016.

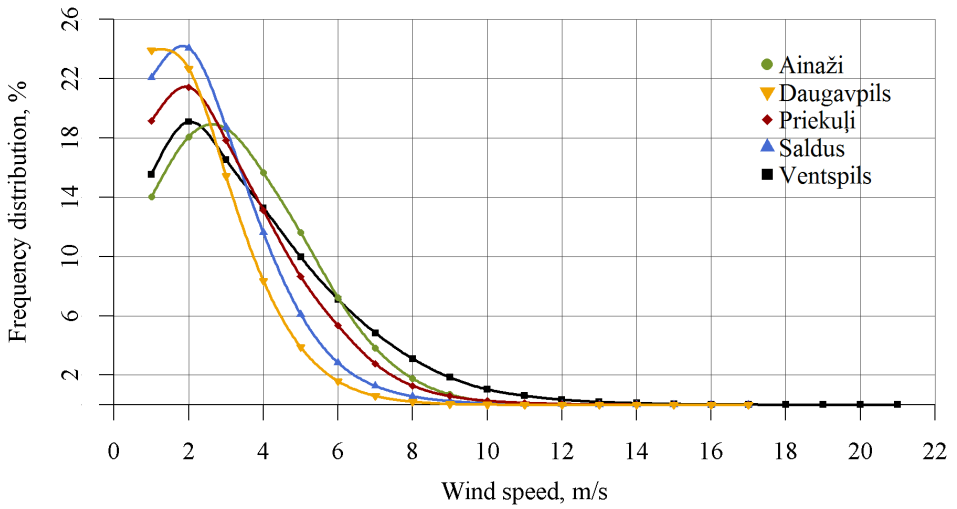

Fig. 5. Frequency distribution functions of average wind speed values V_{avg} *m/s* over the period of observations from 01/01/2015 to 31/12/2016 for 5 meteorological observation stations in Latvia at an altitude of 10 *m* above the ground.

It is important to note that the cubic relationship between the wind energy and its speed results in a situation that wind speed profile that is characterised with bigger displacement to the right typically has higher energy resource potential. In the case of Latvia, distribution functions most displaced to the right frequency correspond to the measurements obtained at Ventspils and Ainaži stations.

Against this background, the density of wind energy for the period of observations can be obtained either by means of summing separate energy quants corresponding to each wind speed bin, or through the use of average cubic speed $V_{avg\ cub}$ in the calculations. In the latter case, the value of average energy density can be expressed as follows:

$$P_{avg} = \frac{1}{2}\rho V_{avg.cub}^3, \tag{3}$$

where

$$V_{avg.cub} = \sqrt[3]{\frac{1}{n}\sum_{i=1}^{n} V_i^3}, \tag{4}$$

where V_i – is the average wind speed with 1 *min* increments, *m/s*;

n – the number of observations of average wind speed for the period of observations;

i – the observation number 1, 2, 3, …, n.

The model of the spatial distribution of average cubic wind speed with the resolution of 1x1 *km* obtained as a result of the interpolation of calculated values is presented in the form of a contour map in Fig. 6.

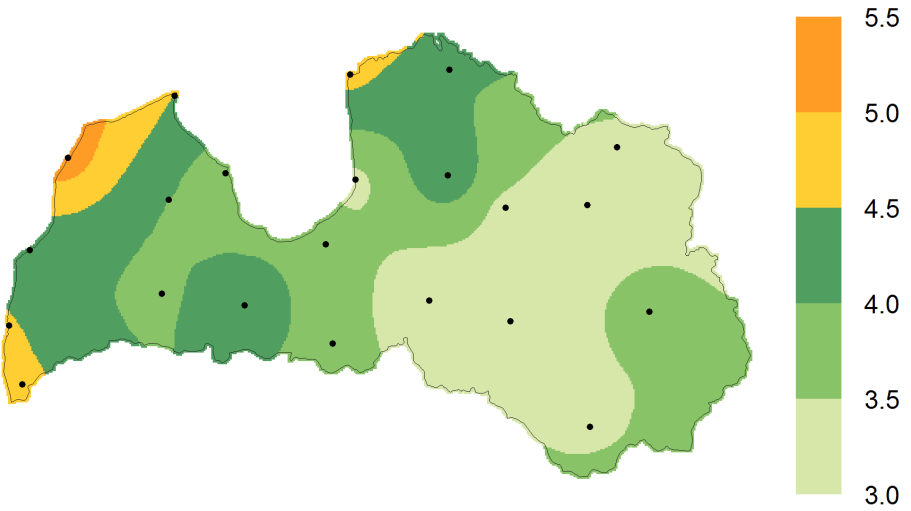

Fig. 6. Model of the spatial distribution of average cubic wind speed *m/s* at an altitude of 10 *m* above the ground in Latvia.

The amount of energy carried by airflow is proportional to the value of the average cubic wind speed (4); therefore, the map in Fig. 6 is equivalent to the density of the wind energy flux, expressed in W/m^2. Moreover, the division of the territory of Latvia into five regions according to the average cubic wind speed can serve as a tool for the comparative evaluation of the resource of wind energy that these regions have.

If the maximum value of average energy density, which wind carries on the shore of the Baltic Sea, is assumed to be 1.0, then the values of the average energy density in relative units for each observation station shown in Fig. 1 will be determined from the following ratio:

$$P'_{avg.i} = V^3_{avg.cub.i} \Big/ V^3_{avg.cub.max}, \tag{5}$$

where $V_{avg.cub.max}$ – the maximum observed value of the average cubic speed at the station in Ventspils region, *m/s*;

$V_{avg.cub.i}$ – the value of average cubic wind speed at each of the 22 observation stations, *m/s*;

i – station 1, 2, 3, …, 22.

As a result of interpolation of the obtained values, a model of the spatial distribution of the mean wind energy density in relative units with a resolution of 1x1 *km* for the territory of Latvia has been compiled. The results of the model are presented in the form of a contour map in Fig 7.

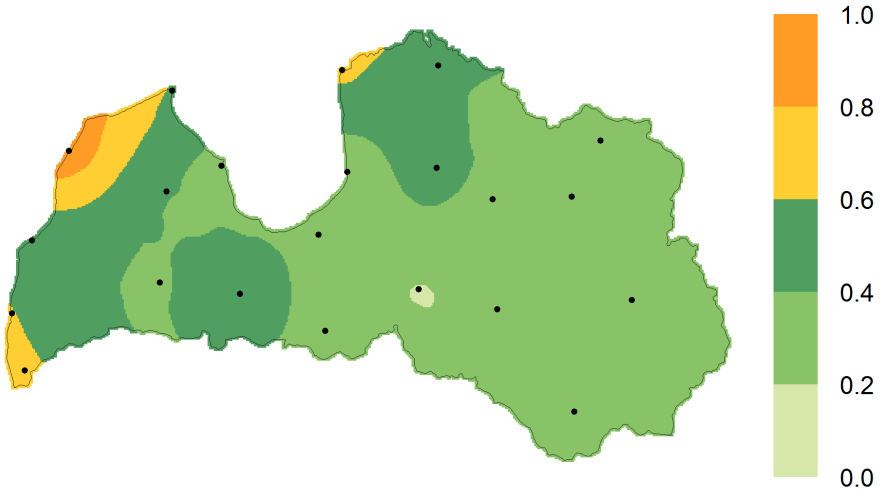

Fig. 7. Model of the spatial distribution of the average wind energy density in relative units at an altitude of 10 *m* above the ground in the territory of Latvia.

Some differences in the distribution of the boundaries of the regions in Figs. 6 and 7 can be attributed to the difference in the scale of the values of the models represented in the figures, corresponding to the and the density of wind energy. For more precise comparison of wind energy intensity in the selected regions of Latvia, Table gives the numerical values of the energy density determined on the basis of the measurements made at meteorological stations.

The visual representation of the distribution of the resource of wind energy on the map makes it possible to predict the efficiency of wind generators with a mast height of 10 *m* on the entire territory of Latvia. Importantly, the map in Fig. 7 shows that in the most of the eastern part of the country the efficiency of wind generators will be three to four times lower than in the western part of the country adjacent to the Baltic Sea.

Table 1

Average Wind Speed V_{avg}, $V_{avg.cub.}$ *m/s* and Wind Energy Density in Relative Units P'_{avg} Obtained as a Result of Physical Measurements at Selected Meteorological Observation Stations and Based on Estimations Using ERA5 Dataset

	Results of measurements			Results of ERA5 modelling			
Station	$V_{avg\ 10m}$, *m/s*	$V_{avg.cub\ 10m}$, *m/s*	$P'_{avg\ 10m}$	$V_{avg\ 10m}$, *m/s*	$V_{avg\ 54m}$, m/s	$V_{avg\ 100m}$, *m/s*	$V_{avg\ 136m}$, *m/s*
Ventspils	4.1	5.4	1.00	6	7.4	8.1	8.5
Ainazi	3.8	4.7	0.66	4.7	6.7	7.2	7.9
Priekuli	3.4	4.5	0.58	3.9	5.5	6.5	7.1
Saldus	3.0	3.9	0.38	3.8	5.3	6.4	6.9
Daugavpils	2.5	3.3	0.23	3.6	4.9	5.9	6.4

5. CONCLUSIONS

The study developed the models of the spatial distribution of wind speed and wind energy density on the territory of Latvia. The models were created on the basis of generalisation of the results of physical measurements of wind speed at an altitude of 10 *m* above the ground.

The models were constructed using the method of spatial interpolation on the basis of measured values and presented in the form of colour contour maps with a 1x1 *km* resolution. Physics measurements were carried out at 22 meteorological observation stations belonging to the LEGMC for a time period from 01/01/2015 to 31/12/2016.

The paper presented the results of an alternative modelling approach towards obtaining the spatial distribution of wind speed using the ERA5 weather modelling technology at the altitudes of 10, 54, 100 and 136 *m* with a 31x31 *km* resolution.

The paper provided the comparative analysis of the results of physical measurements and modelling of average wind speed for meteorological observation stations in Ainazi, Daugavpils, Priekuli, Saldus and Ventspils.

The visual representation of the distribution of wind energy resource presented in the paper makes it possible to estimate the efficiency of wind generators on the whole territory of Latvia.

The developed models of the spatial distribution of wind speed and wind energy can serve as a practical tool and reference material for analysing the prospects of using wind generators in various regions of Latvia and assessing the possibility of commercial use of wind energy at a height of 10 m.

ACKNOWLEDGEMENTS

The research has been carried out within the project "New European Wind Atlas" (NEWA), ENER/FP7/618122/NEWA ERA-NET PLUS, supported by the European Commission under the 7th Framework Programme for Research, Technological Development and Demonstration.

REFERENCES

1. Shipkovs, P., Kashkarova, G., Lebedeva, K., & Migla, L. (2012). Use of renewable energy resources for reduction of environmental pollutions. In the Fourth IASTED African Conference on Power and Energy Systems (AfricaPES 2012), 3–5 September 2012 (pp. 79–85). Gaborone, Botswana. CD Proceedings.
2. Bobinaite, V., & Priedite, I. (2015). RES-E support policies in the Baltic States: electricity price aspect (part II). *Latvian Journal of Physics and Technical Sciences, 2*, 13–25.
3. Bezrukovs, V.P., Bezrukovs, V.V., & Zacepins, A.J. (2014). Comparative efficiency of wind turbines with different heights of rotor hubs: Performance evaluation for Latvia. *J. Phys.: Conf. Ser.* 524 012113. doi:10.1088/1742-6596/524/1/012113
4. Godoy, S., M., & Farret, F.A. (2015). *Modelling and Analysis with Induction Generators* (3rd Edition). CRC Press.

5. Turcik, M., Obuševs, A., Oļeiņikova, I., & Junghans, G. (2013). Assessment of wind production impacts to a power system and market formation in Baltic. *Power and Electrical Engineering*, *31*, 31–37.
6. Vēja karte un kvalitāte. (n.d.) Available at http://www.kerveju.lv/veja_karte.php
7. Ostapenko, J., & Gamalejevs, A. (2004). *Latvian Wind Energy Guide.* Riga.
8. Atjaunojamā enerģija Latvijā. Project No. 2/EEZLV02/ 14/GS/044 Contract No. 2/ EEZLV02/14/GS/044/011 24.04.2015/ Available at http://kpfi.liepu.lv/wpcontent/uploads/2016/03/Renewable_energy_LV.pdf
9. Bezrukovs, V., Zacepins, A., Bezrukovs, V., & Komashilovs, V. (2016). Investigations of wind shear distribution on the Baltic shore of Latvia. *Latvian Journal of Physics and Technical Sciences*, *53*(3), 3–10.
10. ERA5 Public Release 2010-2016. Available at https://climate.copernicus.eu/era5-public-release-2010-2016
11. Bivand, R. S., Pebesma, E. J., & Gómez-Rubio, V. (2008). *Applied Spatial Data Analysis with R* (2nd edition). New York: Springer.
12. Hennermann, K., & Berrisford, P. (2017). ERA5 data documentation. Available at https://software.ecmwf.int/wiki/display/CKB/ERA5+data+documentation
13. Bezrukovs, V., Zacepins, A., Bezrukovs, Vl., & Komashilovs, V. (2016). Comparison of methods for evaluation of wind turbine power production by the results of wind shear measurements on the Baltic shore of Latvia. *Renewable Energy*, *96*, *Part A*, 765–774.
14. Manwell, J. F., McGowan, J. G., & Rogers, A. L. (2009). *Wind Energy Explained: Theory, Design and Application*. John Wiley & Sons Ltd.

VĒJA ENERĢIJAS RESURSU TELPISKĀ SADALĪJUMA MODELĒŠANA LATVIJAS TERITORIJĀ

S. Aņiskeviča, V. Bezrukovs, U. Zandovskis, D. Bezrukovs

K o p s a v i l k u m s

Publikācijā tiek pētīts vēja enerģijas plūsmas telpiskais sadalījums Latvijas teritorijā, kas balstīts uz vēja ātruma novērojumiem 10 *m* augstumā divu gadu periodā – no 2015. līdz 2016. gadam. Ik minūšu novērojumi veikti, izmantojot sertificētas mēriekārtas 22 meteoroloģiskajās novērojumu stacijās, kas pieder Latvijas Vides, ģeoloģijas un meteoroloģijas centram - Latvijas Nacionālajam hidrometeoroloģiskajam un klimatoloģiskajam dienestam. Vidējā vēja ātruma un enerģijas blīvuma telpiskā sadalījuma modelis tika iegūts ar telpiskās interpolācijas metodi, kas balstīta uz novērotajām vērtībām, un attēlots krāsu kontūru karšu veidā ar izšķirtspēju 1 x 1 *km*. Publikācijā tiek sniegti arī vēja ātruma telpiskā sadalījuma modelēšanas rezultāti no klimatiskās reanalīzes ERA5 10, 54, 100 un 136 *m* augstumā ar 31x31 *km* izšķirtspēju. Analīzē ir iekļauts faktisko vēja ātrumu mērījumu salīdzinājums ar ERA5 modelēšanas rezultātiem meteoroloģisko novērojumu stacijās Ainažos, Daugavpilī, Priekuļos, Saldū un Ventspilī.

05.11.2017.

LATVIAN JOURNAL OF PHYSICS AND TECHNICAL SCIENCES
2017, N 6

DOI: 10.1515/lpts-2017-0038

A METHODOLOGY FOR THE ESTIMATION OF THE WIND GENERATOR ECONOMIC EFFICIENCY

G. Zaleskis
Riga Technical University, Faculty of Power and Electrical Engineering, Institute of Industrial Electronics and Electrical Engineering,
12-1 Azenes Str., Riga, LV-1048, LATVIA
e-mail: genadijs.zaleskis@rtu.lv

Integration of renewable energy sources and the improvement of the technological base may not only reduce the consumption of fossil fuel and environmental load, but also ensure the power supply in regions with difficult fuel delivery or power failures. The main goal of the research is to develop the methodology of evaluation of the wind turbine economic efficiency. The research has demonstrated that the electricity produced from renewable sources may be much more expensive than the electricity purchased from the conventional grid.

Keywords: *energy resources, renewable energy sources, wind energy.*

1. INTRODUCTION

Prerequisites of the use of the wind turbine are the following:

- strategic objectives of the use of the renewable energy sources [1]–[3];
- political aspects [4]–[6].

One of the most important economic benefits of wind power is the reduction of economic dependence on fossil fuel. This benefit is substantial enough to justify the expansion of wind energy in several European countries, even if wind energy price per kWh is higher than for other forms of energy production, although this risk reduction is not currently included in the standard methods for the calculation of the energy price [7]. Wind energy price depends on several factors [7]–[9], but, in general, these may be defined as follows: installation and operation costs, operation period and capacity factor.

According to the electricity NET payment system [10] for the microgenerators [11], energy produced by wind turbines can be sold to the conventional power grid operator in accordance with the market price [6], which is variable.

The method for the wind turbine efficiency evaluation was presented in [13]. The aim of present research is to improve the method by specification of used parameters and introduction of new variables. Detailed methodology shall help estimate

the economic efficiency of wind generators in specific conditions.

The market price of electricity is applied equal to 0.065 EUR per kWh, according to [13]. It is also assumed that the necessary energy can be purchased from the grid operator; in this case the price is 0.16 EUR per kWh. For the general assessment of the economic efficiency of wind turbines, the special rules of the grid operator are not taken into account.

According to [14], it was decided [3] that the DC microgrids were necessary for integration of renewable sources. Therefore, the proposed methodology is based on the power relations in the DC microgrid with a wind generator as the main energy source [13].

2. THE MAIN PARAMETERS DESCRIBING POWER FLOWS IN THE WIND ENERGY BASED MICROGRID

The power flows in the alternative energetics microgrid are explained using an example of the DC microgrid, since such configuration is more suitable for the integration of the renewables [15] – [17]. The presented microgrid (Fig. 1) includes the wind turbine producing annually averaged power $P_{w,av}$ which is partially consumed by load with annually averaged power $P_{load,av}$ [13]. The difference of the both powers should be transmitted through the bidirectional converter to the conventional AC grid:

$$P_{grid,av} = P_{w,av} - P_{load,av}, \tag{1}$$

where $P_{grid,av}$ – averaged power transmitted to the grid, W;
$P_{w,av}$ – averaged power produced by the turbine, W;
$P_{load,av}$ – averaged power consumed by load, W.

Wind turbine producing average power is characterised with the capacity factor α, which is the ratio indicator of wind power utilisation during a year:

$$\alpha = \frac{P_{w,av}}{P_{w,r}} < 1. \tag{2}$$

Part of the averaged wind power is consumed by the microgrid load, and its averaged consumed wind power can be characterised with the wind turbine power distribution factor:

$$\beta = \frac{P_{load,av}}{P_{w,av}} = \frac{P_{load,av}}{\alpha \cdot P_{w,r}}. \tag{3}$$

The wind turbine power distribution parameter can be smaller than 1 (and surplus wind energy should be transmitted to the grid) as well as above 1 (when energy flow of the grid supports the needs of consumers).

Using (1), (2) and (3) the power transferred through the conventional grid is:

$$P_{grid,av} = \alpha \cdot P_{w,r} - \beta \cdot P_{w,av} = \alpha \cdot (1-\beta) \cdot P_{w,r}. \tag{4}$$

The specific averaged power of the AC grid is the ratio between the averaged AC grid power $P_{grid,av}$ and the rated power of the wind turbine:

$$P^*_{grid,av} = \frac{P_{grid,av}}{P_{w,r}} = \alpha \cdot (1-\beta) = \alpha - (\alpha \cdot \beta), \tag{5}$$

where $(\alpha \cdot \beta)$ is the specific averaged load power.

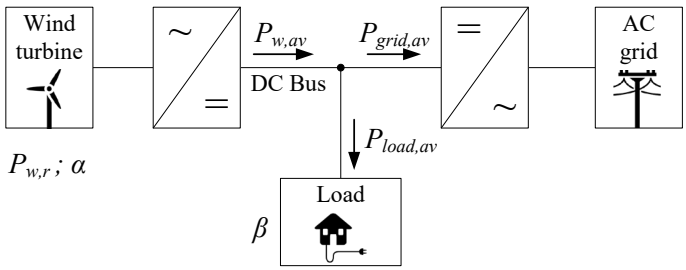

Fig. 1. Power relations in the wind energy based DC microgrid: $P_{w,r}$ – the rated power of the wind turbine; α – the capacity factor; $P_{w,av}$ – the average power of the wind turbine; $P_{grid,av}$ – the average power of the AC power grid; $P_{load,av}$ – the average power of the load; β – the wind power utilisation factor.

According to Fig. 1 and (5), the sign of the AC grid average power $P_{grid,av}$ depends on load power needs and wind turbine generated power. The sign "+" means that surplus of wind energy is transferred to the AC grid; the sign "-" means that load needs of power are in full or in part covered by the AC grid energy.

3. FACTORS INFLUENCING THE PRICE OF THE ENERGY PRODUCED BY WIND GENERATOR

Accepting an approach that annual price of electrical energy produced by the wind turbine can be presented as reduced to the year, as opposed to [18], total annual expenses of wind power [13], [19] plant can be presented as follows:

$$C_w = k_a \cdot C_{kW} \cdot P_{w,r}, \tag{6}$$

where C_{kW} – installation expenses of 1kW installed power of plant, including power converter costs;

k_a – reduction factor for cost of installed power.

Reduction factor k_a [13] characterises possible time duration in years of normal operation T_{op} of the constructed plant as well the relative part k_{exp} of annual operation costs:

$$k_a = \frac{1}{T_{op}} \cdot k_{op}. \tag{7}$$

The actual price of 1 kWh of the produced electrical energy can be calculated as follows:

$$C_{kWh} = \frac{C_{kW} \cdot k_a}{T_{an} \cdot \alpha}, \tag{8}$$

where T_{an} = 8760 is a number of hours in a year.

Thus, the price of the produced wind energy significantly depends on the installation investments and the ratio indicator of wind power utilisation (Fig. 2).

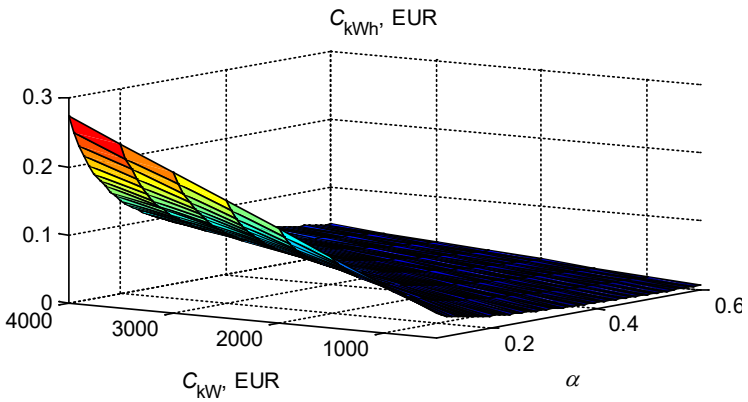

Fig. 2. The price of the energy produced by the wind generator depending on installation investments and capacity factor.

4. COVER OF EXPENDITURE AND REVENUE OPPORTUNITIES

If the AC grid average power $P_{grid,av}$ is positive, the income from electrical energy sales to the conventional grid is observed. In terms of money, this income is equal to:

$$C_{grid} = P_{grid,av} \cdot T_{an} \cdot C_{kWh,market}, \tag{9}$$

where $C_{kWh,market}$ – the market price for the electrical energy, EUR/kWh.

If the AC grid average power $P_{grid,av}$ is negative, the amount of the bought energy in terms of money is equal to:

$$C_{grid} = P_{grid,av} \cdot T_{an} \cdot C_{kWh,grid}, \tag{10}$$

where $C_{kWh,grid}$ – the AC grid operator price for the electrical energy, EUR/kWh.

The AC grid operator price $C_{kWh,grid}$ is higher than the market price because the operator price includes payments for the distribution operator service and the mandatory procurement component. Thus, common economic efficiency of the wind turbine is calculated using the economic efficiency factor of annual energy production $C_{w,com}$:

$$C_{w,com} = C_{grid} - C_w. \tag{11}$$

If $P_{grid,av} \geq 0$ and, accordingly, $\beta \leq 1$, C_{grid} in (11) is calculated as in (9), but if $P_{grid,av} < 0$ and $\beta > 1$, C_{grid} in (11) is calculated as in (10). If $C_{w,com} = 0$, the annual investments in the wind turbine installation, including operating expenses, are equal to income from electrical energy sales to the conventional grid, so if $C_{w,com} > 0$, the profit is stated. There are three cases, when $C_{w,com} < 0$:

- the income from the electrical energy sales is less than annual expenses;
- the generated energy is not on sale to the AC grid;
- there is not enough generated wind energy to provide load demand.

For further calculations it is accepted that normal operation time is 20 years and annual part of the operating expenses is 20 %. Therefore, $k_{exp} = 1.2$ and $k_a = 0.06$ year^{-1}.

The financial efficiency factor of specific annual generation is defined as $C_{w,com}$ and $P_{w,r}$ relation and is equal to:

$$\begin{cases} C^*_{w,com} = \alpha \cdot (1-\beta) \cdot T_{an} \cdot C_{kWh,market} - k_a \cdot C_{kW}, \beta \leq 1 \\ C^*_{w,com} = \alpha \cdot (1-\beta) \cdot T_{an} \cdot C_{kWh,grid.} - k_a \cdot C_{kW}, \beta > 1 \end{cases}. \tag{12}$$

The annual equivalent cost factor depends on the load energy costs at the power grid price:

$$C_{eq} = -P_{load,av} \cdot T_{an} \cdot C_{kWh,grid}. \tag{13}$$

where $C_{kWh,grid}$ – the AC grid operator price for the electrical energy, EUR/kWh.

The specific annual equivalent cost factor is received by reduction of the C_{eq} to the rated power of the wind turbine:

$$C^*_{eq} = -\alpha \cdot \beta \cdot T_{an} \cdot C_{kWh,grid}. \tag{14}$$

If all produced energy is consumed by the load ($\beta = 1$), the financial efficiency factor of specific annual generation is equal to:

$$C^*_{w,com}(\beta = 1) = -k_a \cdot C_{kW}. \tag{15}$$

The energy produced by wind turbines is cheaper than the conventional grid energy, if $C^*_{w,com} > C^*_{eq}$, and this condition depends on α and C_{kW} (Fig. 3).

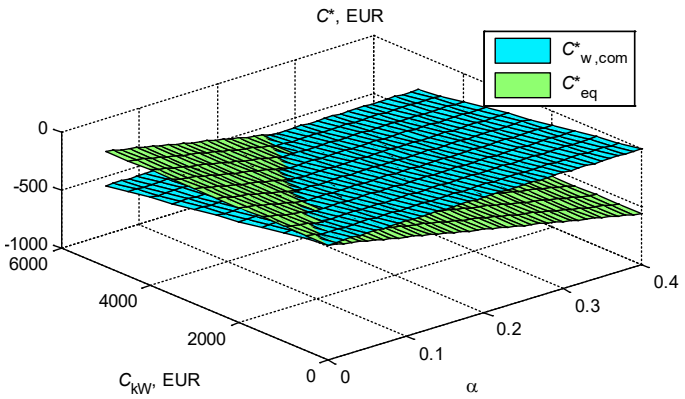

Fig. 3. The financial efficiency factor of specific annual generation comparing to the specific annual equivalent cost factor at $\beta = 1$.

As shown in Fig. 3, there is a minimum necessary value of the capacity factor α_{min}, below which the energy produced by the wind turbine is cheaper than the energy of the conventional grid:

$$\alpha_{\min} = \frac{k_a \cdot C_{kW}}{\beta \cdot T_{an} \cdot C_{kWh,grid}}. \tag{16}$$

If $\beta < 1$ and surplus of the produced wind energy is not transferred to the conventional grid, the minimum load $(\alpha\beta)_{min}$, below which the use of the wind turbine is not economically viable, is defined:

$$(\alpha\beta)_{\min} = \frac{k_a \cdot C_{kW}}{T_{an} \cdot C_{kWh,grid}}. \tag{17}$$

and the minimum value β_{min} of the wind turbine power distribution factor is calculated as follows:

$$\beta_{\min} = \frac{k_a \cdot C_{kW}}{\alpha \cdot T_{an} \cdot C_{kWh,grid}}. \tag{18}$$

If $\beta < 1$ and surplus of the produced wind energy is transferred to the conventional grid, the minimum necessary value of the capacity factor α_{min} is:

$$\alpha_{\min} = \frac{k_a \cdot C_{kW}}{(1-\beta)\cdot T_{an} \cdot C_{kWh,market} + \beta \cdot T_{an} \cdot C_{kWh,grid.}}. \quad (19)$$

If $C_{w,com} \geq 0$, the profit on investments is stated, and the minimum value β_{max} of the wind turbine power distribution factor is defined:

$$\beta_{\max} = 1 - \frac{k_a \cdot C_{kW}}{\alpha \cdot T_{an} \cdot C_{kWh,market}}. \quad (20)$$

5. ESTIMATION OF THE PRICE OF THE PRODUCED ENERGY

The average theoretical generated power of the wind turbine can be calculated using the power curve of the specific wind turbine and actual wind speed diagram (Fig. 4) for the specific period [19]. Calculations were made for the following turbines with similar rated power: VisionAIR5 3.2 kW; Windspot 3.5 kW; Whisper 3.2 kW; Raum Energy 3.5 kW. Estimation of the wind turbine average theoretical power was made by creating the actual wind turbine power diagram for a chosen period and calculating its average value [19]. The example of the power diagram is shown in Fig. 5.

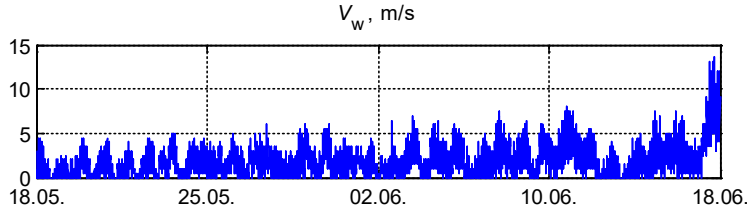

Fig. 4. Wind speed above the building of the Faculty of Power and Electrical Engineering of RTU over the time period from 18/05/2016 to 18/06/2016, average speed is 1.87 m/s.

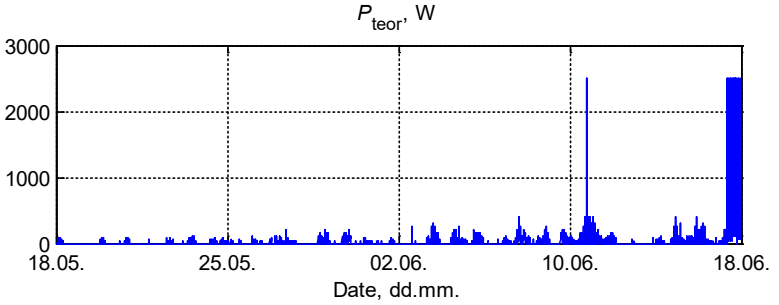

Fig. 5. The theoretical power P_{teor} of the wind turbine VisionAIR5 3.2 kW over the time period from 18/05/2016 to 18/06/2016, average power is 36.1 W.

The measurements of the wind speed (Fig. 4) were made above the building of RTU on Kipsala, Riga (Latvia) at the height of about 30 meters. Using the theoretical average power of the mentioned turbines, the turbine approximate prices, the actual and minimum capacity factors are calculated (Table 1). Table 1 also shows the difference between the price of energy produced by the wind turbine and the price of the conventional grid energy. It is necessary to specify that the calculation was made for a month-long period. The data about the wind speed for a longer period is necessary for more precise estimation.

Table 1

Values of Parameters of Energy Sources

Energy source	Parameters[1]		
	α_{act}	α_{min}	C_{kWh}, EUR
VisionAIR5	0.011	0.321	4.55
Windspot	0.019	0.234	1.97
Whisper	0.030	0.134	0.71
Raum Energy	0.019	0.135	1.08
Conventional grid	N/A	N/A	0.16

Note: α_{act} – the actual capacity factor; α_{min} – the minimum necessary capacity factor; C_{kWh} – the price of 1 kW

6. INFLUENCE OF THE NET PAYMENT SYSTEM ON THE WIND GENERATOR ECONOMIC EFFICIENCY

The influence of the NET payment system [10] on the wind generator economic efficiency was studied in [13] and [19]. The electricity cost for 1 kWh of each Latvian household consists of the three main components: the distribution operator service, the mandatory procurement component (MPC) and the payment for electricity. Each household must paid for operator services and MPC (60 % of the total cost for kWh). Payment for electricity is calculated by the NET principle:

$$E_{net} = E_{grid,cons} - E_{grid,trans}, \tag{21}$$

where E_{net} – the amount of electrical energy for which a household must pay, kWh;
$E_{grid,cons}$ – energy consumed from the conventional grid, kWh;
$E_{grid,trans}$ – energy transferred to the conventional grid, kWh.

Total equivalent amount of electrical energy for which a household must pay is:

$$E_{eq} = 0.6 \cdot E_{grid,cons} + 0.4 \cdot E_{net} = E_{grid,cons} - 0.4 \cdot E_{grid,trans}. \tag{22}$$

The previous research [13], [19] has shown that the payment for electricity depends on the wind energy amount, which was directly consumed by the load without transferring to the conventional grid, and its minimum value is:

$$E_{eq,\min} = 0.6 \cdot E_{grid,cons} = 0.6 \cdot \left(E_{load} - E_{w,cons}\right), \quad (23)$$

where E_{load} – energy consumed by load, kWh;
$E_{w,cons}$ – energy directly consumed from the wind generator.

Considering a probabilistic character of a power source and load [19], the existing rules of the power grid operator complicate the economic calculation of the wind generator. Change in the existing rules can facilitate the integration of renewable energy sources, thus having accelerated implementation of the European Parliament and Council Directives [5] and [6].

7. CONCLUSIONS

The methodology of evaluation of the wind turbine economic efficiency has been developed in the present research. Annual wind turbine usage costs and price of the received energy depend on the capacity factor, which is a ratio indicator of wind power utilisation per year, as well as on the ratio of energy consumed by load to the energy generated by the wind turbine. The efficiency of the wind turbine is evaluated by the use of the generation financial efficiency indicator, which indicates the return of investments (a positive value), losses (a negative value) or the investment and income equality (equal to 0).

The developed methodology of evaluation of the wind turbine economic efficiency can be used for determination of the wind energy price in specific places. The example of the application of the developed methodology for the specific object shows that the produced energy of the 3.2–3.5 kW turbines will be 4.4–28.4 times more expensive than the conventional grid energy. The calculation was made for a month-long period. The data about the wind speed for a longer period is necessary for more precise estimation.

The economic effect of the utilisation of the wind turbines depends on the conventional grid operator regulations and the electricity payment system, which determine a possibility for a wind turbine owner to get compensation for energy transferred to the grid. The analysis of the electricity NET payment system in Latvia has been made within the framework of the research. To describe the financial efficiency of the wind turbine, the indicator E_{eq} (total equivalent amount of electrical energy for which a household must pay) has been used. The payment for electricity depends on the wind energy amount, which was directly consumed by the load without transferring to the conventional grid. The smallest value of the equivalent energy can be reached at the maximum possible energy amount generated by the wind turbine and the energy amount directly consumed by load.

ACKNOWLEDGEMENTS

The research has been supported by the Latvian National Research Programme LATENERGI.

REFERENCES

1. Latvijas Republikas Vides aizsardzības un reģionālās attīstības Ministrija. (2006). Atjaunojamo energoresursu izmantošanas pamatnostādnes 2006.–2013. gadam (informativa dala), Rīga.
2. Adamovičs, A., Dubrovskis, V., & Plūme, I. (2009). Biomasas izmantošanas ilgstspējības kritēriju pielietošana un pasākumu izstrāde. Rīga: Valsts SIA Vides projekti.
3. Zaleskis, G., & Steiks, I. (2016). Alternative energetics dc microgrid with hydrogen energy storage system. *Electrical, Control and Communication Engineering*, *11*, 21–26.
4. Zaleskis, G., Steiks, I., Pumpurs, A., & Krievs, O. (2015). DC-AC converter for load supply in autonomous wind-hydrogen power system. In 56th International Scientific Conference on Power and Electrical Engineering of Riga Technical University (RTUCON), 14 October 2015 (pp. 169–173). Riga: RTU Press.
5. Directive 2009/28/EC of the European Parliament and of the Council on the promotion of the use of energy from renewable sources. (2009). Official Journal of the European Union, L 140/16.
6. Directive 2010/31/EU of the European Parliament and of the Council on the energy performance of buildings. (2010). Official Journal of the European Union, L 153/13.
7. Krohn, S., Morthorst, P.-E., & Awerbuch, S. (2009). *The economics of wind energy*. European Wind Energy Association.
8. Moné, C., Smith, A., Maples, B., & Hand, M. (2015). *2013 cost of wind energy review*. National Renewable Energy Laboratory: Golden CO.
9. Gadonneix, P., Nadeau, M.-J., Kim, Y. D., Birnbaum, L., Cho, H.-E., Choudhury, A.R. … Frei, C. (2013). *World energy perspective*. World Energy Council.
10. Electricity NET payment system. [Online]. Available at http://sadalestikls.lv/eng/klientiem/pieslegumi/mikrogeneratoru_pieslegums/electricity_net_payment_system/
11. Microgenerator connection. [Online]. Available athttp://sadalestikls.lv/eng/klientiem/pieslegumi/mikrogeneratoru_pieslegums/
12. Elektrum Dinamiskais and the market price. [Online]. Available at https://www.elektrum.lv/en/for-business/for-customers/ elektrum-dinamiskais-and-the-market-price/
13. Zaleskis, G., & Rankis, I. (2016). Problem of an estimation of the wind generators economic efficiency in Latvia. In Proceedings of the 20th International Conference ELECTRONICS 2016 (pp. 16–21), Kaunas, Lithuania.
14. Bunker, K., Doig, S., Hawley, K., & Morris, J. (2015). *Renewable microgrids: Profiles from islands and remote communities across the globe*. Rocky Mountain Institute and Carbon War Room.
15. De Doncker, R. W. (2012). *Future DC grid technology for more decentralized power production and renewable power supplies*. IEEE PEDG2012.
16. Graillot, A. (2009). *Hybrid micro grids for rural electrification: Developing appropriate technology*. Maputo: Trama TecnoAmbiental.
17. Karlsson, P. (2002). *DC distributed power systems*. Ph.D. Thesis, Lund University.
18. International Renewable Energy Agency. (2012). *Renewable energy technologies: Cost analysis series*, 1.
19. Zaleskis, G. (2017). Research of the automation tasks of the wind generators in the low-power microgrids. Ph.D. Thesis (in Latvian), Riga: Riga Technical University.

VĒJA ĢENERATORU EKONOMISKĀS EFEKTIVITĀTES NOTEIKŠANAS METODOLOĢIJA

G. Zaļeskis

K o p s a v i l k u m s

Atjaunojamo enerģijas resursu integrēšana un to tehniskās bāzes uzlabošana var ne tikai veicināt neatjaunojamu enerģijas resursu patēriņa un ekoloģiskās slodzes samazināšanu, bet arī nodrošināt elektroapgādi reģionos ar apgrūtināto kurināmo piegādi vai elektroapgādes traucējumiem. Pētījumā mērķis ir izveidot metodoloģiju vēja turbīnu ekonomiskās efektivitātes noteikšanai. Pētījums parādīja, ka noteiktos apstākļos elektroenerģija, kas tika iegūta no atjaunojamiem avotiem, var būt krietni dārgāka par iepirkto no centralizētā tīkla enerģiju.

07.11.2017.

LATVIAN JOURNAL OF PHYSICS AND TECHNICAL SCIENCES
2017, N 6

DOI: 10.1515/lpts-2017-0039

NEW HYDROKINETIC TURBINE FOR FREE SURFACE GRAVITATIONAL WAVE TRANSFORMATION

J. Berins
Faculty of Power and Electrical Engineering, Riga Technical University1 Kalku Str., Riga, LV-1658, LATVIA

The present article deals with an alternative form of energy – the conversion of marine/ocean wave energy using an axial self-regulating blade (SB) hydrokinetic turbine (ASRBHK turbine). The article analyses the operation of the ASRBHK turbine and draws the resulting conclusions about the mechanism, in which the power transfer element is a self-regulating blade.

Keywords: *axial hydrokinetic turbine, renewable energy, wave energy, wave energy power plant, wave energy converter, wave energy receiver, self-regulating blade*

1. INTRODUCTION

The total amount of wind-generated wave energy is less than the total amount of wind power in the world, due to the fact that only part of the wind power transfers to the waves. As wind-generated wave energy accumulates, there can be significantly more energy in the aquatorium than in the same area in the air above it.

Sea and ocean waves are potential and perspective renewable energy sources – estimates of the global wave energy potential are between 8,000 TWh and 80,000 TWh per year [1]. In order to achieve this goal, it is necessary to create new, efficient equipment for the construction of wave energy power plants. At least 140 scientific institutions working on wave energy transformation issues have been involved in around 200 different projects since 2000 [2]. In spite of this fact, it is still urgent to find the most effective way of converting wave energy into rotational motion for powering electric generators. Let us look at one of the following options – *APRLHK* turbine. The article will provide insight into *APRLHK* turbine operation in a wave environment.

The aims of the article are to evaluate the principle of the axial hydrokinetic turbine with self-regulating blades, to create the receiver's operation and to draw conclusions from its analysis.

2. A SHORT DESCRIPTION OF WAVE PHYSICS

Salt water weight per m^3 is slightly over 1 ton. This indicator varies in different water areas and changes even in the same place. This is the density of the volume

of water which, affected by the Earth's gravitational force in the wind created free surface wave, varies in time and space in a particular way. Looking at the surface of the water, there are characteristic changes in the wave surface, such as period, amplitude, wave length, wave phase and wave group velocity.

The motion of particles in the deep wave is shown in Fig. 1. Particle motion decreases with increasing depth; therefore, the amount of power and energy decreases. It is assumed that the energy in the deep-wave is up to depth equal to half the length of the wave [3]. With increasing depth, the amount of energy decreases exponentially. Therefore, about 95 % of the wave energy is up to depth equal to ¼ of the length of the wave.

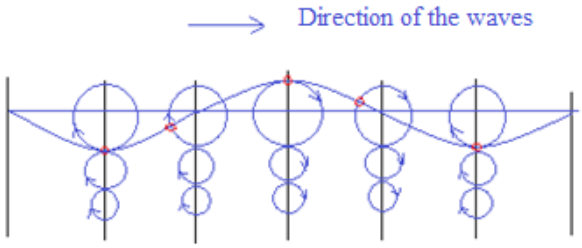

Fig. 1. Particle movement in the wave.

3. A BRIEF OWERVIEW OF WAVE ENERGY EQUIPMENT

In order to absorb and reduce wave energy, i.e., to reduce the amplitude and velocity of its particle movement, a converter is required. It is a three-dimensional body to which the wave reacts. The wave has a specific direction of expansion and action in different phases.

As a result, the spatial body moves or deforms in a manner determined by the receiver's construction and the degree and or form of its elemental freedom.

Particle movement in wave construction – the degree and / or form of its elemental freedom, deformation determines how much energy will be reflected and how much of it will be consumed by treating the wave while moving the absorber surfaces.

According to this theory, a simple point-absorber, moving up / down, spends part of the energy generating radial waves and, thus, is capable of absorbing no more than 50 % of the wave energy [4]. The shape of the receiver is the designer's choice, and the wave absorption / conversion coefficient in water is theoretically 100 % [5] (unlike air, in which it does not exceed 59 % according to Betz criterion), [6].

Machines that completely stifle waves and, thus, wave energy tend to be called wave terminators. In literature, there are also the following names: Salter's Duck [7], Evans or Bristol Cylinder [8]. It is possible that the Cycloidal wave energy converter [9] may also be counted as such (as do all terminators that have a frequency-dependent efficiency curve). An oscillating water column with a resonance chamber, in which, as the direction of the water flow changes, the direction of rotation of the hydro turbine does not change, because the turbine blades are either swivelable [10], in two directions, TWO-WAY tilting blades, or have servomotor controlled blade

angles [11]. Stage of readiness of the prototype at a scale 1: 1.5 [12], at D = 6m is a declared efficiency 8 to 30 % in technology development. The machine is designed in two versions:

1. As a "static" fixed to a stand, the shore, or wind generator mast;
2. As a floating design with 4 "slings".

A test prototype (at scale X: Y) power 4.5 kW Ecofys Wave Rotor, Ocean Mill is a vertical axis velocity boost turbine, whose productivity is supplemented by the Wells hydro turbine wave to capture the kinetic energy of the vertical component [13]. CycWec is a cross-flow turbine with two blades, but unlike the Darius turbine it has a horizontal axis, an angle of inclination of steerable blades and a controllable wave detection angle [14]. Fixing / anchoring methods – a mast or floating frame. Total efficiency coefficient of electricity generation is 15 %. The developer suggests that by improving the blade profile it is possible to achieve an efficiency coefficient of up to 70 %.

4. APRLHK TURBINE TECHNICAL SOLUTION

Because of the fact that it is possible to achieve similar shapes with *SB*, as with classical hydrokinetic turbines, we design and view the *ASRBHK* turbine, which would be more suitable for changing a wave direction and changing load conditions (see Fig. 2). The *ASRBHK* turbine consists of a vertical fixed axis *"A",* a flywheel *"FW"*; turbine blades *"SB",* spindles *"SP"* and bearings *"B"* (see Fig. 2). The axis *"A"* shown in Fig. 2 is fixed rigidly in the vertical position to prevent the turbine wheel from moving up and down and sideways. It provides the maximum effect of wave forces on *SB*. The *SP* holds the longest edge of the *SB* tensioned (see Fig. 3 – marked with a red line), thus promoting the transfer of wave forces to the turbine wheel in all *SB* positions. Figure 3 shows three *SB* positions (*P1, P2* and *P3*) demonstrating the *SB* states and the effect of water particles (indicated by the speed vertical and horizontal components v_n and h_n) on it. With the abbreviation *"TB",* Fig. 3 illustrates the *SB* bearing structure or the turbine branch, but with *"SB"* – the self-adjusting blade.

The density of salt water can be 1030 kg m3 or more. In the case of turbine moving parts (*SB*), it is better if their volume is as close to the volume of the water they work in as possible, so as to reduce the negative effect of additional gravity or lift on wave power transfer efficiency. Therefore, a significant indicator is the average value of water density in the aquatorium.

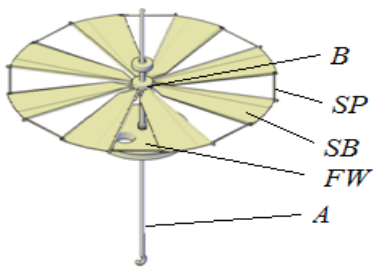

Fig. 2. Sketch of the *ASRBHK*.

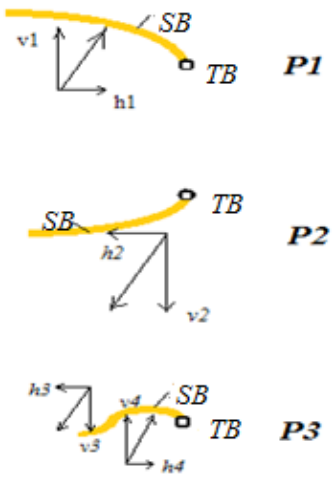

Fig. 3. Water particle effect on *SB*.

5. ASRBHK TURBINE OPERATION TESTS AND THEIR RESULTS

In order to test the *ASRBHK* turbine, a model for work in a laboratory was made, where the parameters of incoming and outgoing waves (Frequency γ, Hz and amplitude *A*, m) were measured and data were obtained by receiving signals from laser sensors. The signals then arrived at the data analyser and, using special software, they were archived and processed by creating a wave analysis scheme (see Fig. 4). One dominant wave direction was taken – in the direction of a wave generator to a wave-energy receiver. Due to reflection, the tidal wave and waves, the direction of which coincided with the initial wave, arose for this direction of waves [15]. Measurements were made following a specific measuring structure and optical circuitry [15]. A chronometer was used to measure turbine speeds at different braking loads of the driving pulley as well as without load. Load was put on the flywheel *"SK"* (see Fig. 2) by winding a cord around it and changing its strain strength (*F*) which was read using a dynamometer. As the strength changed minutely, we used video surveillance during the tests. This made it possible to capture variations in the force according to time and to calculate its average value. The indicators w (angular velocity, rps.) were calculated from the speed of the fixed receiver n and the test time t, s, obtained with the chronometer. The loading arm, m, which is equal to the flywheel radius *r*, was measured with a tape measure. Some of the most significant parameters used in the relationships (*w, F* and *r* – measured, *v, P, P (AK)* and η – calculated) are shown in Table 1. *P* – the power dissipation *W* was calculated using the equation:

$$P = v \cdot F, \tag{1}$$

where P – power, W;
v – speed, m/s;
F – force, N.

Let us calculate velocity v from the measured angular velocity w:

$$v = w \cdot \pi 2r/t, \tag{2}$$

where t – time, s;

w – angular velocity, rps;

π – constant of the circle line;

r – loading arm, m.

and $P\ (AK)$ the wave power calculated from the obtained wave parameter measurements of (3), [3]:

$$P(AK) = \frac{\varphi g H^2 c_g b}{8}, \tag{3}$$

where $P\ (AK)$ – calculated wave power before receiver, W;

f – water weight, kg/m^3;

g – free fall acceleration, m/s^2;

H – mean wave height, m;

c_g – wave group speed, m/s;

b – the wave-width to be detected, m.

As the experiment was performed in freshwater, in a laboratory, we assumed that the weight of the water was 1000 kg / m3, the free fall acceleration $g \sim 9.81$ m / s^2, $H = 2A$, where the measurement method for amplitude A was described in [15], but test data were archived using a specially designed computer program and the received wave width was 0.90 m, which was equal to the receiver diameter.

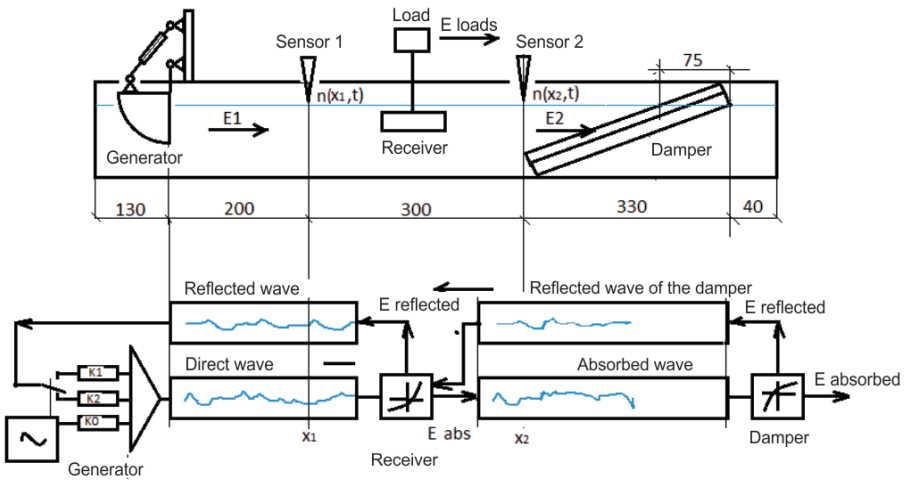

Fig. 4. Wave process analysis scheme [15].

Table 1

Measured and Calculated Parameters of the Tests

w, rps	F, N	r, m	v, m/s	P, W	P (AK), W	w, rps	η, %
-	1.628	0.15	-	-	1.472	-	-
0.03	1.218	0.15	0.03	0.04	1.462	0.03	2.62
0.05	1.099	0.15	0.05	0.05	1.483	0.05	3.49
0.08	0.809	0.15	0.08	0.06	1.424	0.08	4.46
0.12	0.541	0.15	0.11	0.16	1.491	0.12	3.99
0.17	-	0.15	0.16	-	1.474	0.17	-

In deep-water conditions, the group wave velocity is expressed as follows [3]:

$$c_g = c/2, \tag{4}$$

where

c – wave speed, m/s.

Wave speed is expressed as follows [3]:

$$c = \frac{gT}{2\pi}, \tag{5}$$

where g – free fall acceleration, m/s^2;

T – wave period, s;

π – constant of the circle line.

Wave frequency was measured during the test. Therefore, in the calculations of wave speed c, we used (6):

$$\gamma = \frac{1}{T}, \tag{6}$$

where γ – wave frequency oscillation per second;

T – wave period, s.

To determine the *ASRBHK* turbine efficiency, we used (7):

$$\eta = \frac{P}{P(BK)} \cdot 100\ \%, \tag{7}$$

where η – efficiency factor, %;

P – turbine load capacity, W;

$P\ (AK)$ – wave energy, W.

The efficiency coefficient curve of mechanically tensioned *ASRBHK* turbine, under laboratory conditions, is shown in Fig. 5.

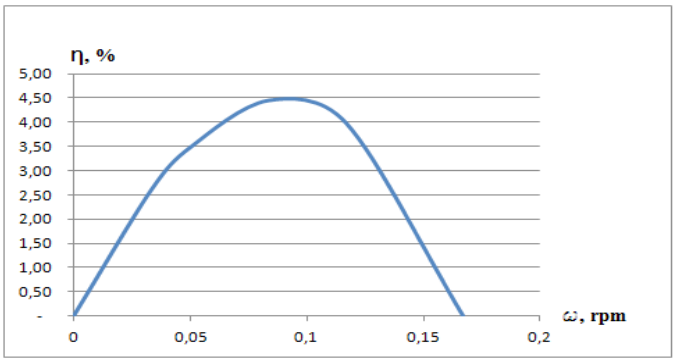

Fig. 5. The efficiency coefficient curve of mechanically tensioned *ASRBHK* turbine.

6. ASRBHK TURBINE PERFORMANCE ANALYSIS

From the *SB* positions *P1, P2* and *P3* in Fig. 3, which exist in three different wave phases, we can see that:

a. In position *P1*, the vertical component of the forces generated curves the *SB* upwards, but the horizontal component – in the direction of rotation of the turbine;
b. In position *P2*, the vertical component of the forces generated pushes the *SB* downwards, while the horizontal component moves it counter to the direction of rotation of the turbine and produces an increased hydraulic resistance in the curved *SB* surface;
c. In position *P3, SB* is simultaneously in two wave phases and the effects of wave particles characteristic of one and the other wave phases are acting accordingly.

Let us look at the forces at work on the temporarily free form blade (see Figs. 7 and 8). The blade bearing structure is marked with *"B"*. The vertical component of the velocity of the water particles is the force acting on the *SB* and is shown in the top left corner of Fig. 7, but how it will act on *SB* – with different shades (the darker the stronger the effect) of blue and red (depending on the direction of action – up with red or down with blue) below, where three *SB* positions (*P1, P2* and *P3*) are displayed. Figure 6 shows one static moment in which the wave crosses *ASRBHK* turbines *SB*. In addition, it is assumed that the wavelength is equal to the length of the blade to better highlight the phenomenon that occurs in *SB* in the wave environment. However, be aware that real wavelengths will vary, they may be shorter or longer than *SB*. Figure 6 also shows the direction of the *ASRBHK* turbine rotation with angular velocity w and horizontal direction of travel. The horizontal component of the wave energy also acts on the *ASRBHK SB*. This effect is shown in Fig. 8. The direction of the horizontal flow in blue is in the direction of the wave (the darker the colour, the more intense the flow), but red – in the opposite direction.

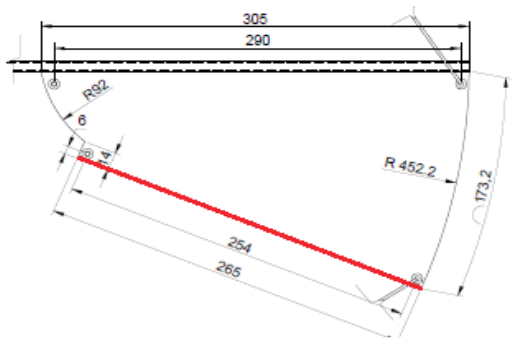

Fig. 6. Self-regulated blade of turbine *(SB)*.

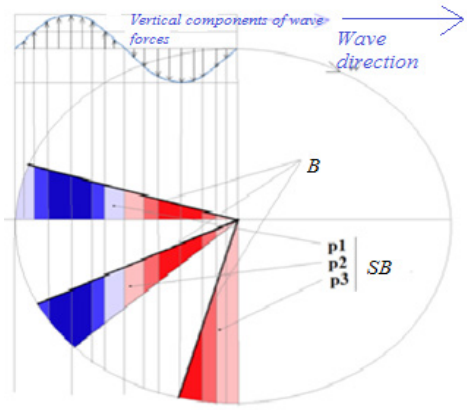

Fig. 7. Scheme for the propagation of vertical forces on the *ASRBHK* turbine *SB*.

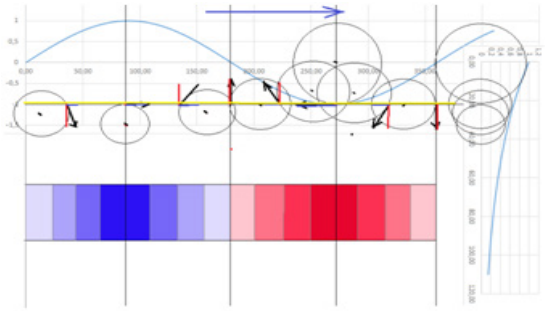

Fig. 8. The effects of the horizontal components of the wave force on the *ASRBHK* turbine *SB*.

7. CONCLUSIONS

1. The *ASRBHK* turbine (see Fig. 2) is capable of turning the variable directional flow in the direction of rotation, due to the *SB* sails functionality.
2. When operating in *SB* rotation around the vertical axis, it simultaneously falls into it, but not only with opposing forces. This reduces the effectiveness of *SB* operations.

3. In order to increase the efficiency of *SB*, technical solutions are needed to ensure that *SB* is continuously positioned perpendicularly to the direction of wave movement.
4. Moving parallel to the wave direction of motion, *SB* receives the wave forces more efficiently, since they are in different wave phases for a shorter period of time.

7. FUTURE RESEARCH

A mechanism must be developed that ensures the *SB* position is perpendicular to the direction of the waves and complimented by the energy potential of the target aquatorium of the power plants. The algorithm for calculating the size of the equipment must be developed by proceeding from the wave parameters characterising the aquatorium. It is necessary to modify or develop material for industrial equipment *SB*.

ACKNOWLEDGEMENTS

This article and article "Mesurements of wave power in wave energy converters effectiveness evaluation" *(Latv. J. Phys Tech. Sci., 2017, Vol. 54 Iss 4, pp. 23-35) have been written in accordance with contract No. 1.2.1.1/16/A/005 between Competence Center of Smart Materials and Technologies Ltd. and the Central Finance and Contracting Agency, concluded on 26 September 2016, the study is conducted by SensoTech Ltd. with support from the European Regional Development Fund (ERDF) within the framework of the project "Competence Center of Smart Materials and Technologies".*

REFERENCES

1. Holmberg, H., Anderson, M., Bolund, B., & Stananger, K. (2011). *Wave Power, Surveillance Study of the Development.* Elforsk rapport 11: 02.
2. Berins, J., Grickus, A., & Kalnacs, A. *Wave Energy Conversion-Overview and Perspectives*. Available at http://site-11936.mozfiles.com/files/11936/Wave_enrgy_conversion_publication_2a.pdf
3. McCormick, M.E. (2007). *Ocean Wave Energy Conversion*. New York: Dover Publications Inc.
4. Falnes, J. *Principles for Capture of Energy From Ocean Waves. Phase Control and Optimum Oscillation*. Department of Physics, NTNU. Available at http://folk.ntnu.no/falnes/web_arkiv/InstFysikk/phcontrl.pdf
5. Evans, D. V. (1976). A theory for wave-power absorptionby oscillating bodies. *Journal of Fluid Mechanics*, *77*, 1–25.
6. Betz, A. (1920). Das maximum der theoretisch m¨oglichen ausn¨utzung des windes durch windmotoren. *Zeitschrift f¨urdas gesamte Turbinenwesen*, *26*, 307–309.
7. Salter, S. H. (1989). World progress in wave energy-1988. *International Journal of Ambient Energy,10*(1), 3–24.

8. Evans, D. V., Jeffrey, D. C., Salter, S. H., & Taylor, J.R. M. (1979). Submerged cylinder wave energy device: Theory and experiment. *Applied Ocean Research, 1*(1), 3–12. Available at http://oregonwave.org/oceanic/wp-content/uploads/2014/10/Oregon-Incubator-Stefan-Seigel.pdf
9. Grases, G.M., & Grases, M.J.M. (2013). *Hydraulic turbine having pivoting blades for the bidirectional use of fluids.* Patent No. WO2013021089A2. Available at http://google.com/patents/WO2013021089A2?cl=en
10. Grases, G.M., & Grases, M.J.M. (2013). *Hydraulic turbine having pivoting blades for the bidirectional use of fluids*. Patent No. 2013021089 A3. Available at http://google.com/patents/WO2013021089A3?cl=en
11. Fundación Repsol. (2014). *Sendekia presents its prototype at the RTC*. Available at http://www.fondoemprendedores.fundacionrepsol.com/en/up-to-date/news/sendekia-presents-its-prototype-rtc
12. Scheijgrond, P.C. (2009). *Device for the utilisation of wave energy and a method*. Patent US 20110198849 A1. Available at https://www.google.ch/patents/US20110198849
13. Siegel, S.G. (2014). Cycloidal wave energy converter. Development progress and outlook. *Ocean Renewable Energy Conference IX*. Available at http://oregonwave.org/oceanic/wp-content/uploads/2014/10/Oregon-Incubator-Stefan-Seigel.pdf
14. Berins, J., Berins, J., & Kalnacs, A. (2017). Measurements of wave power in wave energy converter effectiveness evalution. *Latvian Journal of Physics and Technical Sciences*, 54(4), 23–35.

HIDROKINĒTISKA TURBĪNA BRĪVAS VIRSMAS GRAVITĀCIJAS VIĻŅU PĀRVEIDOŠANAI

J. Beriņš

K o p s a v i l k u m s

Raksts ir par vienu no alternatīvās enerģijas veida – jūras/okeāna viļņu enerģijas pārveidošanu ar aksiālu pašregulējošu lāpstiņu (PL) hidrokinētisko turbīnu (APRLHK turbīna). Raksta devums ir APRLHK turbīnas darbības analīze un no tās izrietošie secinājumi par to, kādam jābūt mehānismam, kurā spēka pārneses elements ir pašregulējoša lāpstiņa.

19.10.2017.

LATVIAN JOURNAL OF PHYSICS AND TECHNICAL SCIENCES
2017, N 6

DOI: 10.1515/lpts-2017-0040

PERFORMANCE EVALUATION OF IRBENE RT-16 RADIO TELESCOPE RECEIVING SYSTEM

M. Bleiders, Vl. Bezrukovs, A. Orbidans
Engineering Research Institute "Ventspils International Radio Astronomy Center" of Ventspils University College, Inzenieru str., 101, Ventspils, LV-3601, LATVIA

In the present paper, recent measurement results of refurbished Irbene RT-16 radio telescope receiving system performance are presented. The aim of the research is to evaluate characteristics of RT-16, which will allow carrying out necessary amplitude calibration in both single dish and VLBI observations, to improve the performance of existing system as well as to monitor, control and compare performance if possible changes in the receiving system will occur in future. The evaluated receiving system is 16 m Cassegrain antenna equipped with a cryogenic receiver with frequency range from 4.5 to 8.8 GHz, which is divided into four sub-bands. Multiple calibration sessions have been carried out by observing stable astronomical sources with known flux density by using in-house made total power registration backend. First, pointing offset calibration has been carried out and pointing model coefficients calculated and applied. Then, amplitude calibration, namely antenna sensitivity, calibration diode equivalent flux density and gain curve measurements have been carried out by observing calibration sources at different antenna elevations at each of the receiver sub-bands. Beam patterns have also been evaluated at different frequency bands. As a whole, acquired data will serve as a reference point for comparison in future performance evaluation of RT-16.

Keywords*: amplitude calibration, pointing calibration, radio astronomy*

1. INTRODUCTION

Ventspils International Radio Astronomy Centre (VIRAC) radio telescope RT-16 at Irbene has recently been upgraded with new mirror, tracking and reception systems, which have already been verified in multiple astronomical observations during the year 2017, including successful Very Long Baseline Interferometric (VLBI) sessions in European VLBI Network (EVN), and multiple types of single dish observations, including Active Galactic Nucleus (AGN) and spectral line monitoring. To improve the performance of RT-16 in both VLBI and single dish modes, multiple calibration sessions have been carried of which the main results are described in subsequent sections. First of all, evaluation and compensation of beam pointing errors have been carried out. Secondly, optimum feed horn position at secondary focus has been found. Then, the main characteristic parameters of radio telescope have been

evaluated, which include antenna gain elevation dependence, system temperature and beam patterns. Performance has been evaluated at frequencies of 4.5 to 8.8 GHz, which is frequency range of RT-16 main receiver divided into four sub-bands that are designated as C1 to C4 in this paper. For the reference, the main parameters of RT-16 system are summarized in Table 1.

Table 1

Summary of RT-16 Radio Telescope System

REFLECTOR SYSTEM	
Diameter of primary mirror	16 m
Diameter of secondary mirror	1.6 m
Distance of primary base to secondary focus	2.095 m
f/D of primary mirror	0.3
Subtended angle at secondary focus	34°
Surface error of primary mirror	635 μm RMS [6]
Half power beam width	C1: 0.26° or 16 arcmin, C2: 0.21° or 13 arcmin C3: 0.20° or 12 arcmin, C4: 0.16° or 10 arcmin
TRACKING SYSTEM	
Az/El range	-328 to +328° / 2.5 to 94°
Az/El maximum velocity	5/4 °/s
Az/El maximum acceleration	1.5/2 °/s/s
Az/El tracking accuracy	3.3 arcsec /3.3 arcsec
RECEIVER SYSTEM	
Frequency range	4.5 to 8.8 GHz
Frequency ranges of available sub-bands and frequency of corresponding local oscillator	C1: 4500 – 5500 MHz, LO = 4100 MHz C2: 5400 – 6400 MHz, LO = 5000 MHz C3: 6400 – 7600 MHz, LO = 6100 MHz C4: 7600 – 8800 MHz, LO = 7300 MHz
Polarization	Right and Left Circular Polarizations
Calibration functionality	Noise source injection and VLBI phase cal. system
Available signal registration back-ends	DBBC2/Mark5c, Total power meter and Spectrum analyzer

2. CALIBRATION OF POINTING ERRORS

Before it is possible to carry out any observations, it is necessary to characterize pointing errors because it is not possible to rely solely on constant tracking system encoder offsets due to potential secondary mirror or feed displacements, gravitational deformations, axis misalignment etc. which may also be dependent on antenna elevation and azimuth. To characterize pointing errors, multiple applications included in VLBI Field System (FS) were employed [1] in combination with in-house made total power meter which was integrated in FS as a station detector for this purpose. Measurements were carried out mostly in C3 band (see Table 1) with bandwidth of 1200 MHz as it was reasonably high frequency and clean from radio

interference. To measure pointing offsets at particular antenna position, application FIVPT was used, which implemented discrete point cross-scans in both azimuth and elevation axis across the astronomical point source and linear-Gaussian function fitting algorithm to calculate offsets.

Multiple 12 to 24 hour long pointing calibration sessions were carried out to acquire pointing offsets at different antenna position angles by cross-scanning bright point sources 3C123, 3C84, 3C461 (CasA), 3C405 (CygA), 3C144 (TaurusA), 3C145 (OrionA) and 3C454.3. For data acquisition control FS AQUIR application was used. Here we present results of recent calibration session, carried on 28 July, 2017. Total of 213 points were acquired with sky coverage shown in Fig. 2. For more uniform coverage a source list must be increased, which may not be feasible with a current cross-scan algorithm because source fluxes may be too weak in case of RT-16 to obtain reliable results. Weather conditions during the session were good, with clear sky and low wind.

To compensate for azimuth and elevation dependent pointing offsets, the model is fit on the raw offset data, which afterwards is used to calculate offset at any antenna position. In this case, we were employing FS pointing model, which was based on 23 antenna physical parameter model described in [2]. To obtain parameters of the model FS PDPLT application was used. Results together with raw data are visualized in Fig. 1.

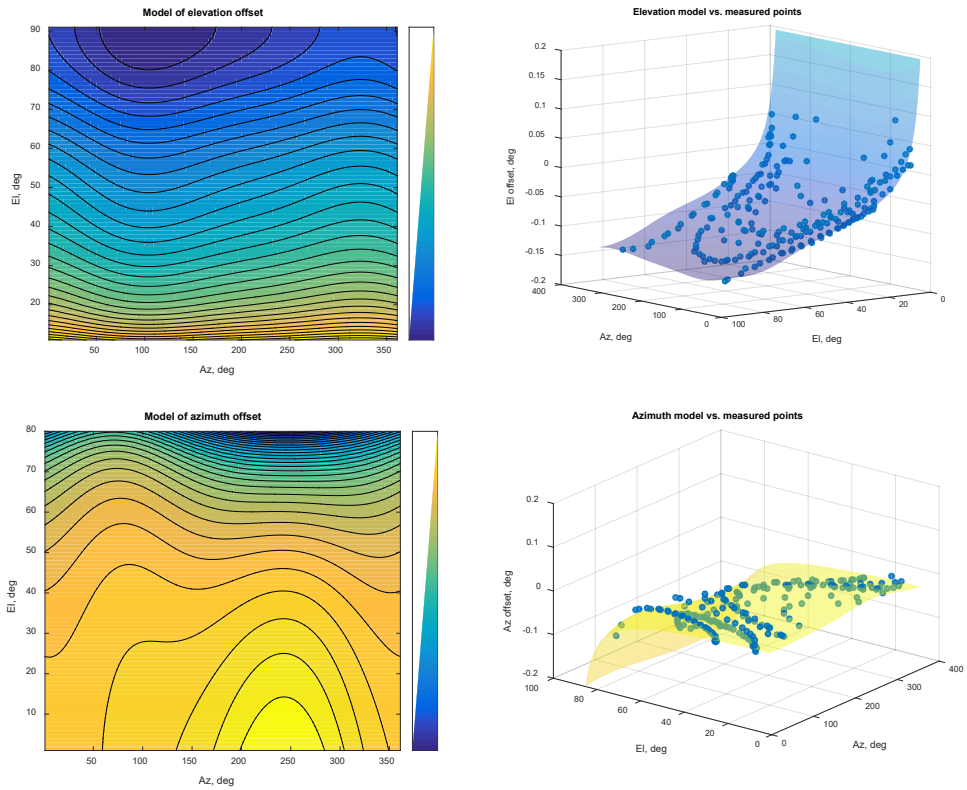

Fig. 1. Derived pointing models of RT-16 and raw data points (28 July, 2017).

There is relatively large elevation offset dependence on elevation present with maximum amplitude of ≈0.15° which is almost 100 % of Half Power Beam Width (HPBW) at highest frequency band (C4 – 8400 MHz) of RT-16. It may be explained with possible secondary mirror gravitational sag, which is also evident in antenna beam patterns (see Fig. 9) In the case of azimuth offsets, dependence on elevation and azimuth is relatively flat up to elevations of ≈65° where at higher angles offsets start to increase. Interestingly, there is some kind of hysteresis present, which can be noticed in bottom right plot of Fig. 1. In other words, at higher elevations, azimuth offset values differ at almost the same azimuth and elevation positions – the only known difference is being direction of antenna slew for those points. Due to this issue and combination with small sky coverage at higher elevations, accuracy of azimuth model is poor above elevations of 70° and must be investigated more thoroughly. Overall statistics of current pointing model are shown in Table 2. Pointing model was verified by carrying out successive calibrations session, results of which could be compared in Fig. 2 and Fig. 3.

Table 2

Residuals of Pointing Model Shown in Fig. 1

Azimuth RMS residual: 0.015° (54”), Max error: 0.039° (140”)
Elevation RMS residual: 0.0065° (23.4”), Max error: 0.021° (76”)

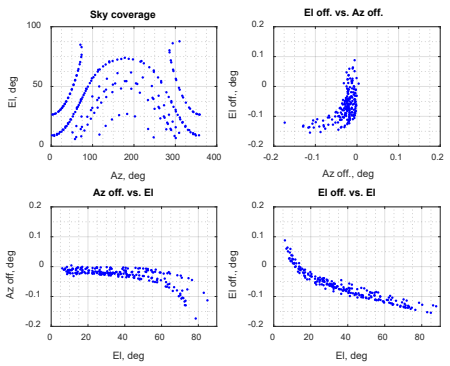

Fig. 2. Pointing errors of RT-16 before applying the pointing model.

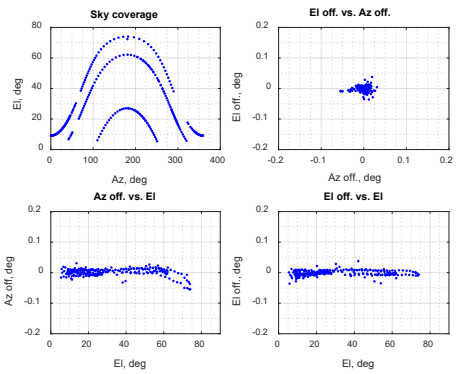

Fig. 3. Pointing errors of RT-16 after applying the pointing model.

3. BASICS OF AMPLITUDE CALIBRATION

In general, radio telescope amplitude calibration can be described using following equations [3]:

$$Tcal[Jy] = S_f[Jy] \cdot \frac{TP_{cal} - TP_{sky}}{TP_{src} - TP_{sky}} \quad (1)$$

$$Tcal[Jy] = \frac{Tcal}{DPFU(El)} \cdot e^{\tau * AM} \quad (2)$$

$Tcal[Jy]$ - Calibration diode noise in Jy;

$S_f[Jy]$ - Source flux density in Jy. Assumed to be constant and known;

TP_{cal} - Measured power with beam off source and cal. diode on;

TP_{sky} - Measured power with beam off source and cal. diode off;

TP_{src} - Measured power with beam on source and cal. diode off;

$Tcal$ - Cal. diode noise density in K. Assumed to be constant and known;

$DPFU(El)$ - Elevation dependent antenna gain in Degrees Per Flux Units, K/Jy;

τ - Atmospheric zenith opacity;

AM - Air mass coefficient. $AM \approx \frac{1}{\sin(El)}$.

Calibration noise equivalent flux density *Tcal[Jy]* can be directly measured, by comparing total power increment caused by injected noise diode signal and observed source with known flux. *Tcal[Jy]* is dependent on calibration noise source signal power and antenna gain, which can be calculated using (2), if calibration diode noise density in Kelvins is known. Depending on observation frequency and weather conditions atmospheric absorption term $e^{\tau * AM}$ has to be taken into to account. In case of relatively low available frequencies of RT-16 receiver, atmospheric absorption becomes noteworthy only at elevations below ≈10°, but attention should be devoted if observing in C4 band and/or weather conditions are not optimal. Basically, one only needs to know *Tcal[Jy]* to calibrate raw data to absolute flux units, but separating the system noise and gain from the equation (see (3), (4)) is useful for characterizing and monitoring the antenna and receiver subsystems of telescope separately.

4. DETERMINATION OF OPTIMAL FEED HORN POSITION

RT-16 C band receiver includes a linear actuator system which allows axially moving the feed horn assembly in total range of 650 mm to fine tune its position in secondary focus and facilitate the maintenance. Although optimum position of the feed was already roughly known, more accurate measurement was carried out. 6.7 GHz methanol maser W3OH was chosen as a reference source for gain measurement, which increased measurement accuracy and speed, because signal amplitude could be measured without physically moving the beam off the source. Measurement was carried out with automated read-back of spectrum analyzer marker values while tracking the source and at the same time moving the feed horn from lower position at 0 to upper position at 650 mm. To calibrate receiver gain variations, calibration noise diode was switched during the measurement. Signal spectrum during the measurement process and equations used for gain calculation are outlined in Fig. 4. Marker M1 represents the on-source signal – automatic peak tracking was turned on for M1 to compensate for any Doppler shift during the measurement which might be significant if similar measurement were carried out in timescales of few hours. Average of M2 and M3 represents the off-source signal and frequency positions these markers were chosen experimentally to be maximally close to the spectral line. Total measurement time was 11 minutes which was limited by actuator movement speed and

total elevation change during the measurement was only from 38° to 37° so elevation dependence of gain and system temperature could be neglected. System temperature and gain (in form of DPFU) were calculated according to equations (3), (4) derived from rearranging (1), (2). Results are shown in Fig. 5.

$$T_{sys} = T_{cal} \cdot \frac{TP_{sky}}{TP_{cal} - TP_{sky}} \tag{3}$$

$$DPFU = \frac{T_{sys}}{S_f} \cdot \frac{TP_{src} - TP_{sky}}{TP_{sky}} \tag{4}$$

T_{sys} - system temperature, K;
$DPFU$ - gain, K/Jy;
T_{cal} - calibration noise temperature, K;
S_f - calibration source flux, Jy;
TP_{cal} - <M2,M3> with cal diode on;
TP_{sky} - <M2,M3> with cal diode off;
TP_{src} - M1 with cal diode off.

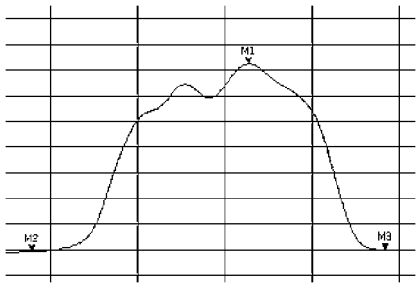

Fig. 4. Gain measurement using methanol spectral line W3OH source.

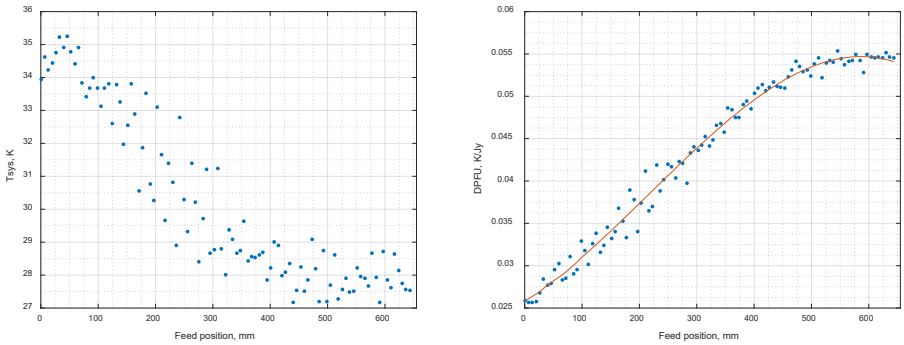

Fig. 5. System temperature and DPFU dependence on axial position of RT-16 feed antenna measured at 6700 MHz.

Measurement results show that not only DPFU varies with feed position, but also decreases when feed is in upper position which could be explained with less noise pickup from secondary cone walls in comparison with case when feed is fully

shifted inside the cone. Right graph of Fig. 5 shows that maximum gain is reached when feed is at 650 mm position and judging from flatness of the response at that point, this is the optimum position. It should be noted that this measurement was carried only at 6.7 GHz due to availability of spectral line sources. For maximum confidence, similar measurements would have to be carried out at rest of the sub-bands to determine if any compensation were needed due to frequency dependence of feed antenna phase center position, probably using ONOFF method and continuum sources. However, seeing the flat response at the focus point at 6.7 GHz, gain loss due to a focusing error at lower frequency bands should not be much increased.

5. MEASUREMENT OF ANTENNA GAIN

To determine the antenna gain of RT-16 at different sub bands and more importantly its dependence on elevation or gain curves, position switched measurement procedure based application ONOFF provided by FS was used for measurement of *Tcal[Jy]* from which the gain in form of DPFU was derived using (2). Multiple calibration sessions were carried out to measure gain at all four sub bands and both polarization channels. Total power measurement was carried out in full bandwidth of the sub-band (≈1200 MHz). FS AQUIR application was used to collect the data at different antenna elevations by observing sources with the known flux density. Sources 3C123, 3C196, 3C295, 3C286 were used as flux calibrators with flux scales adapted from [5]. As an exception, 3C84 was used at measurement of gain curve at C4 band because of its relatively high brightness which allowed decreasing the scatter of the data. Weather conditions during the measurements were good, with clear sky, expect it was overcast during the C4 band measurement. During the measurement, the pointing model described previously was applied. No opacity corrections were applied. Example of measurement results together with raw data points for C1 are shown in Figure 6 and curves for all bands are shown in to Figure 7. Third order polynomial function was fit on the measured data points and could be used to calculate elevation dependent DPFU in (2) using (5). Polynomial coefficients for all sub bands are shown in Table 3.

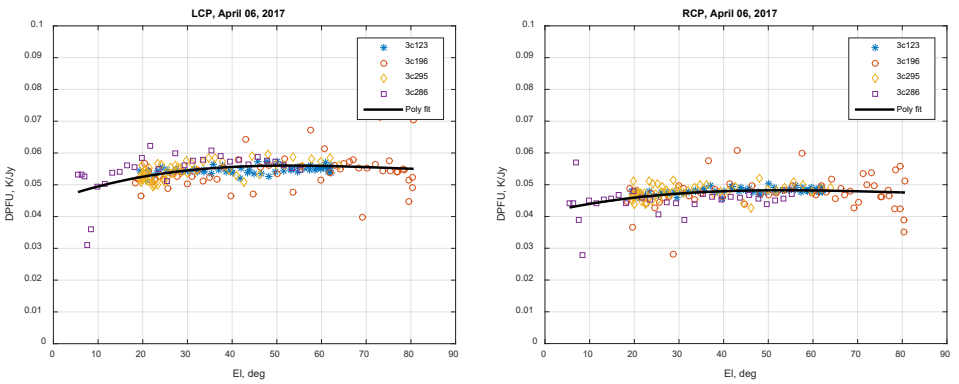

Fig. 6. DPFU dependence on elevation at C1 (5000 MHz) sub band.

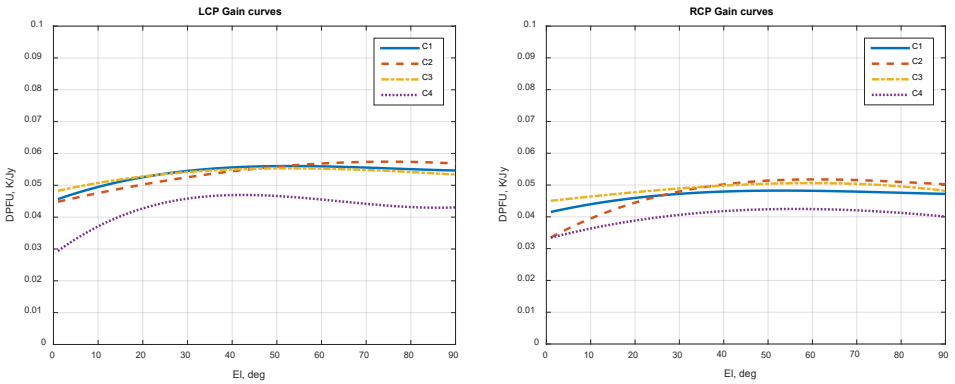

Fig. 7. Gain polynomial curves for C1 to C4 sub-bands.

$$DPFU(El) = DPFU \cdot (a_3 \cdot El^3 + a_2 \cdot El^2 + a_1 \cdot El + a_0) \quad (5)$$

Table 3

Gain Curve Polynomial Coefficients for RT-16 at C1 to C4 Sub-bands

Sub b.	Pol	T_{cal}, K	DPFU, K/Jy	a_3	a_2	a_1	a_0
C1	RCP	50.34	0.0484	3.94E-07	-8.20E-05	5.36E-03	8.88E-01
	LCP	50.34	0.0550	1.50E-07	-3.57E-05	2.61E-03	9.40E-01
C2	RCP	45.01	0.0510	1.38E-06	-2.66E-04	1.59E-02	6.95E-01
	LCP	45.01	0.0552	-1.15E-07	-6.22E-06	2.19E-03	9.15E-01
C3	RCP	41.29	0.0506	-2.23E-07	-5.26E-06	3.00E-03	8.87E-01
	LCP	41.29	0.0553	2.48E-07	-7.39E-05	5.73E-03	8.67E-01
C4	RCP	31.16	0.0432	6.20E-07	-1.67E-04	1.24E-02	7.20E-01
	LCP	31.16	0.0479	2.58E-06	-4.14E-04	1.96E-02	7.03E-01

The obtained gain curves are relatively flat at all bands which are expected from light antenna surface and relatively low frequencies of RT-16 C band receiver. No pronounced maximum is present, but gain tends to increase at higher elevations which may be explained by fact that panels of primary surface were adjusted in zenith position. Consistently increased DPFU is observed in LCP channel at all bands, which may be a result of inaccurate values which were assumed to be the same for both polarization channels and must be determined in the future using hot-cold absorber calibration. No major absolute value differences are present between the sub-bands, expect for the C4 where reduced gain was observed, which should be verified after calibration of .

6. SYSTEM TEMPERATURE AND OPACITY

Additional outcome of ONOFF measurement is system temperature T_{sys} which can be calculated using (3). As absolute values are highly dependent on weather conditions and knowledge of T_{cal}, the following data should be considered as approximate and is useful for relative comparison only. Elevation dependence of T_{sys}

at different sub-bands were measured during the amplitude calibration sessions described in last section and example for C1, C4 sub bands is shown in Fig. 8.

It can be noticed that absolute values of T_{sys} are different between polarization channels which may be due to insufficient knowledge of T_{cal}. In all sub bands response is relatively flat down to elevations of ≈45°, where it starts to increase due to increase of atmosphere absorption and antenna spillover. Data of T_{sys} elevation dependence or the so called "skydip" measurement allows calculating zenith opacity τ which can be used to compensate atmospheric absorption according to (2). Steps of determining the opacity are outlined in [3] and [5]. Table 4 shows opacity determined from data shown in Fig. 8. Value shown for each sub band is average between both polarization channels. Opacity is increasing with increasing frequency as it is expected, but more frequent measurement should be carried to conclude if atmospheric absorption should be compensated in RT-16 C band astronomical data.

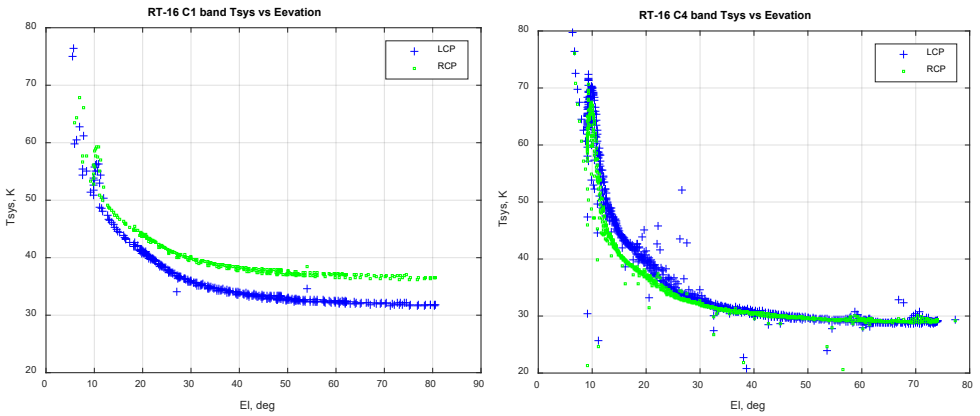

Fig. 8. Elevation dependence of RT-16 system temperature at C1, C4 sub-bands.

Table 4

Zenith Opacities at Different Sub-bands Measured during April to August, 2017. Weather Conditions: Clear Skies Expect Overcast in C4 Sub-band

Sub-band	C1 5000 MHz	C2 6100 MHz	C3 6700 MHz	C4 8400 MHz
Zenith opacity	0.0156	0.0163	0.0176	0.0262

7. BEAM PATTERNS

To evaluate any large-scale errors of RT-16 reflector system, beam pattern measurements were carried out. Sensitivity of RT-16 is sufficient to measure first side lobes using bright astronomical sources, which can tell about feed, secondary mirror misalignments and large scale deformations of primary mirror. Automated raster scanning and data acquisition script was made for this purpose. In this case

'Z' type offset scanning was carried out while tracking the point source. Total power meter was used for signal registration in full ≈1200 MHz IF bandwidth of RHC channel. 3C405 was used as a point source, total measurement time for each pattern was about 30 minutes and during this time maximum antenna elevation change was about 5°. No amplitude calibration was done, so results were useable as rough estimate of beam shape. Measured (26 July, 2017) beam patterns at C1 and C4 sub-bands are shown in Fig. 9.

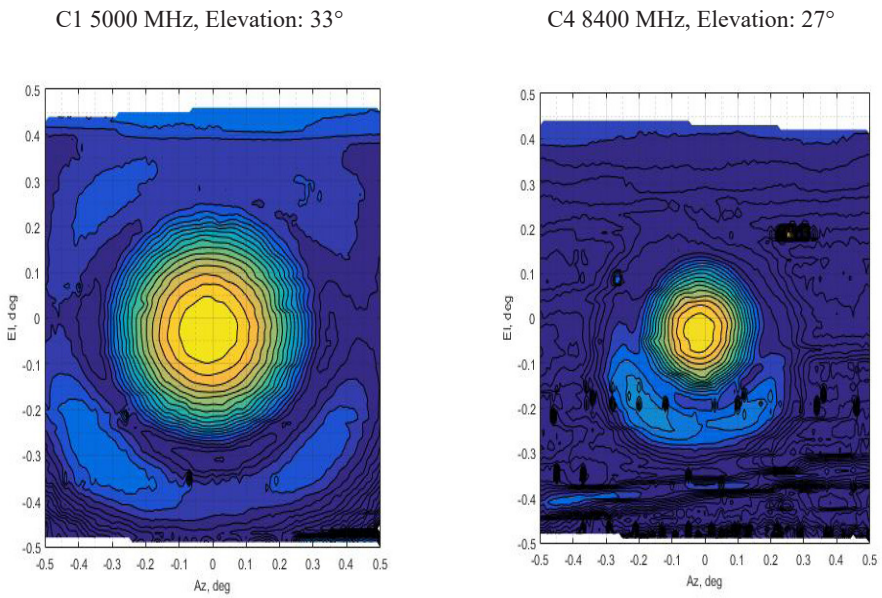

Fig. 9. Estimated beam patterns of RT-16 at C1 and C4 sub-bands.

Asymmetry of first side lobes are visible, which indicates lateral shift in secondary mirror or large-scale deformation of primary surface, of which last is very unlikely given the light, newly installed mirror structure. Increased amplitude in lower side of the beam indicates that secondary mirror may be laterally shifted downwards in elevation. In this case offset of the main lobe should be in positive Y direction – the shown patterns are centered on the main lobe due to a pointing model being applied during the measurements. It explains elevation dependent negative valued elevation offsets shown previously in this report and would mean that secondary mirror shift was dependent on elevation. Similarity of lobe shape in different elevations may indicate that there is a constant component of secondary shift present, which after correction could improve the performance even in case of elevation dependence. Concluding from gain curve measurements, influence of elevation dependent component of lateral shift on antenna gain is very small which is expected for small shifts relative to wavelength, but more rigorous tests should be carried out to better understand this issue. Main lobe width and side lobe offset is decreasing with increasing frequencies as it is expected. To increase the quality of measurements and allow comparing relative levels of side lobes with simulated values, amplitude calibration of the data must be carried out.

8. SUMMARY OF SENSITIVITY PERFORMANCE

Table 5 summarizes the sensitivity performance of RT-16 receiving system at different sub bands. DPFU and T_{sys} values are given in assumption that T_{cal} is known. Ratio of T_{sys} over DPFU or system effective flux density (SEFD) is a direct result from amplitude calibration source observations and should be more accurate. Gain relative to isotropic antenna and figure of merit values are derived from DFPU and SEFD measurements. The obtained efficiency values reasonably well match theoretically approximated values of 0.787 to 0.806 provided in manufacturer documentation of RT-16 [6]. Lower values may be explained with possible secondary mirror displacement, but it must be again verified after calibration of T_{cal}.

Table 5

Summary the RT-16 Sensitivity Performance

Sub band	Center freq, MHz	Pol	Tsys, K (Zenith)	DPFU, K/Jy (Max)	G, dBi (Max)	eff_A (Max)	SEFD, Jy (Zenith)	G/Tsys, dB (Zenith)
C1	**5000**	RCP	34.37	0.048	56.67	0.66	712.27	41.31
		LCP	29.89	0.056	57.32	0.77	533.34	42.37
C2	**6100**	RCP	28.79	0.052	58.71	0.71	556.14	44.11
		LCP	32.13	0.057	59.16	0.79	559.54	44.09
C3	**6700**	RCP	28.90	0.051	59.42	0.69	570.95	44.81
		LCP	31.38	0.055	59.81	0.76	567.31	44.84
C4	**8400**	RCP	29.27	0.043	60.65	0.59	684.90	45.99
		LCP	29.32	0.048	61.11	0.65	616.76	46.44

9. CONCLUSIONS

First overall performance evaluation of Irbene RT-16 radio telescope receiving system has been carried out, which may serve as a reference for future evaluation. Pointing calibration has been carried out to correct azimuth and elevation pointing errors to overall RMS of 54” and 23” respectively by employing the Field System pointing model. More efficient cross-scan algorithm should be implemented to allow for more uniform sky coverage of data in shorter period of time and utilization of weaker sources which will result in better accuracy of the current model. More rigorous characterization of azimuth offsets above elevations of 70° and azimuth offset dependence on direction of antenna slew must be carried out. Antenna gain measurements show relatively small dependence on elevation, which is expected. There is difference in both gain and system temperature values, which may be the result of insufficient knowledge of calibration noise diode temperature and should be verified after calibration of T_{cal}. Nevertheless, the gain curve coefficients and *Tcal[Jy]* ratios are measured for all four sub-bands of RT-16 receiver, which may serve for amplitude calibration of astronomical data. Beam pattern evaluation shows increased lower side lobe level which indicates possible lateral shift of secondary mirror. Given the large elevation dependent elevation offsets, it may be concluded

that secondary shift results from elevation dependent gradational influence on the secondary mirror. Overall measured figure of merit values in form of SEFD and G/T_{sys} are as expected considering the new high performance antenna and receiver and it is clear that apart from small mirror displacement no major performance limiting issues are present in the system.

REFERENCES

1. Himwich, W. E. (1993). NVI, Inc./GSFC, Antenna Calibration Programs - *VLBI Field System Documentation. NASA/Goddard Space Flight Center.*
2. Himwich, W. E. (1993). NVI, Inc./GSFC, Pointing Model Derivation - *VLBI Field System Documentation. NASA/Goddard Space Flight Center.*
3. Kraus, A. (2013). MPIfR, Calibration of Single Dish Telescopes. *ERATec Workshop, Bologna.*
4. Kraus, A. (2007). MPIfR. Calibration of the Effelsberg 100m telescope.
5. Perley, R. A., & Butler B. J. (2013). An Accurate Flux Density Scale from 1 to 50 GHz. *The Astrophysical Journal Supplement Series, DOI: 10.1088/0067-0049/204/2/19*
6. MT Mechatronics. (2015). *Report VTP2-DOC-11210-02: Assessment of the RT16 antenna surface performance and illumination efficiency.*

IRBENES RADIO TELESKOPA RT-16 UZTVEROŠĀS SISTĒMAS VEIKTSPĒJAS NOVĒRTĒJUMS

M. Bleiders, Vl. Bezrukovs, A. Orbidāns

K o p s a v i l k u m s

Šajā rakstā tiek prezentēti nesen renovētā Irbenes radioteleskopa RT-16 uztverošās sistēmas veiktspējas mērījumu rezultāti. Šī darba mērķis bija novērtēt RT-16 uztverošās sistēmas parametrus, kas ļautu veikt novērojumu datu amplitūdas kalibrēšanu vienas antenas un VLBI režīmos, uzlabot esošās sistēmas veiktspēju, kā arī monitorēt un salīdzināt veiktspēju iespējamu sistēmas izmaiņu gadījumā. Apskatītā uztverošā sistēma ir 16 m Kasegrēna tipa paraboliskā antena, kas aprīkota ar platjoslas kriogēni dzesēto uztvērēju ar frekvenču diapazonu no 4.5 līdz 8.8 GHz, kas sadalīts četrās apakš joslās. Ir veiktas virkne kalibrēšanas sesijas, novērojot astronomiskos avotus ar stabilu un zināmu intensitāti, izmantojot institūtā izstrādātu pilnās jaudas reģistratoru. Pirmkārt, tika veikti antenas stara pozicionēšanas nobīžu mērījumi, kas ļāva aprēķināt pozicionēšanas modeļa koeficientus. Pēc tam veikta amplitūdas kalibrācija, kas ietver teleskopa jutības, kalibrācijas trokšņu diodes ekvivalento intensitāti un pastiprinājuma līknes, veicot kalibrācijas avotu mērījumus dažādās antenas elevācijas pozīcijās. Papildus tam, novērtētas antenas virzības diagrammas visos četros frekvenču apakš diapazonos. Iegūtie rezultāti kalpos kā atskaites punkts, novērtējot RT-16 veiktspēju nākotnē.

10.11.2017.

LATVIAN JOURNAL OF PHYSICS AND TECHNICAL SCIENCES
2017, N 6

DOI: 10.1515/lpts-2017-0041

APPLIED PHYSICS

NUMERICAL APPROACH OF A WATER FLOW IN AN UNSATURATED POROUS MEDIUM BY COUPLING BETWEEN THE NAVIER–STOKES AND DARCY–FORCHHEIMER EQUATIONS

K. Hami[1,2], I. Zeroual[1]
[1]Institute of Science and Technology,
University Center of Tindouf, Tindouf, 37000, ALGERIA
[2]Laboratory of Energetic in the Arid Areas ENERGARID,
Faculty of Technology, University Tahri Mohammed, Béchar, 08000, ALGERIA
hamikhelifa@yahoo.fr

In the present research, simulations have been conducted to determine numerically the dynamic behaviour of the flow of underground water fed by a river. The basic equations governing the problem studied are those of Navier–Stokes equations of conservation of momentum (flows between pores), coupled by the Darcy–Forchheimer equations (flows within these pores). To understand the phenomena involved, we first study the impact of flow rate on the pressure and the filtration velocity in the underground medium, the second part is devoted to the calculation of the elevation effect of the river water on the flow behaviour in the saturated and unsaturated zone of the aquifer.

Keywords: *Darcy–Forchheimer equations, groundwater flow, hydrodynamic modelling, porous medium*

1. INTRODUCTION

The particularity of the reinforcements considered in the research is the presence of several scales of porosity. On the one hand, the flow is modelled in the pores by the law of Darcy–Forchheimer, and on the other hand, it is modelled between the pores by the Navier–Stokes equations. The authors of the research, therefore, have a domain containing both a porous medium and a fluid zone.

This problem has already been studied for a long time, since Beavers and Joseph [1] study the flows of Navier–Stokes and speak already in their introduction about extensive analytical literature. They show the existence of the velocity of slip on the surface of the porous environment and propose a boundary condition. Thereafter, Saffman [2] justified this boundary condition mathematically and showed that the term velocity of Darcy could be neglected. It thus gave the condition known under the name of condition of Beavers–Joseph–Saffman. Certain digital studies concerning the coupling of the equations of Stokes and Darcy take into account this boundary condition, while others do not consider it.

Many authors have coupled the Navier–Stokes equations for the fluid area and Darcy's equation for the porous zone. Correa and Loula [3] propose a coupling between a Navier–Stokes finite element formulation and a Darcy mixed formulation using Taylor-Hood elements.

J. M. Urquiza et al. [4] have presented a mixed finite element formulation of the Navier–Stokes with a formulation of the equation of Darcy taken in the form of a Poisson's equation.

G. Pacquaut et al. [5] express the weak formulation of each equation by integrating the condition of Beavers–Joseph–Saffman. Taking into account the boundary conditions being common to each formulation, they could inject the equation of Darcy directly in the formulation of Navier-Stokes, which allowed for the coupling. In principle, this makes the weak formulation of the equation of Brinkman.

G. N. Gatica et al. [6] use also a coupling of (Navier–Stokes)–Darcy equations to compare several types of elements to achieve a stable formulation. Once again, the resolved wording finally returns a weak formulation of the Brinkman equation. Masud [7] makes the same type of study by clearly solving the Brinkman equation, which he writes under his strong formulation, but calling it the Navier–Stokes–Darcy equation.

H. Tan and K. M. Pillai [8] also propose a finite element formulation of the Brinkman equations. However, they propose a modified Brinkman equation to take into account a stress jump at the fluid-porous interface.

The coupling between the equations of Darcy and Navier–Stokes was largely studied before by using the finite volume method (FVM) in the immersion of fields, because of the many applications utilising the heat transfer in the porous environments and to the interface between the porous environment and the external fluid [9]–[10]. The technique of immersion of fields used was improved thereafter [11]–[14].

2. SIMULATION PROCEDURES

2.1. Mathematical Model

The equations which govern the problem treated (2) (3) and (5) are those of Navier–Stokes (flow between the pores) coupled by the Darcy–Forchheimer equations (flows inside these pores) expressing respectively the conservation of mass and momentum.

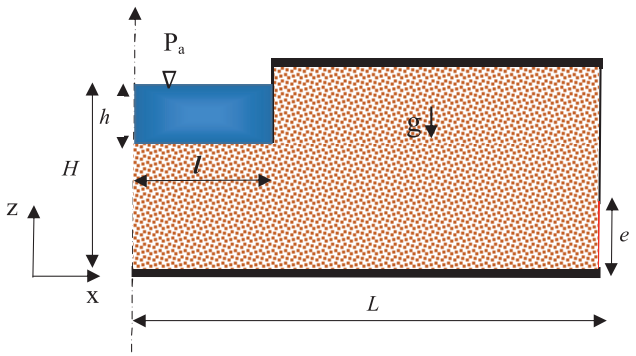

Fig. 1. Physical model.

(H = 50 m, L = 100 m); (h = 5 m, l = *20* m); e = 10 m.
$P_a = 10^5$ Pascal.

2.1.1. Equation: Porous Jump

$$\Delta p = -\left(\frac{\mu}{\alpha} + C_2 \frac{1}{2}\rho v^2\right)\Delta m \tag{1}$$

where μ is the dynamic fluid viscosity, Δm is the thickness of the medium coefficient, v is the velocity normal to the porous face, α is the permeability of the medium and C_2 is the pressure jump coefficient. α, Δm and C_2 are parameters of boundary conditions specified by the user. In laminar flows through porous media, the pressure drop is typically proportional to velocity and the constant C_2 can be considered to be zero, ignoring convective acceleration and diffusion.

2.1.2. Equation: Continuity

$$\frac{\partial u}{\partial x} + \frac{\partial w}{\partial z} = 0 \tag{2}$$

The equation is obtained by considering the mass flux into a representative elementary volume *(R.E.V)* to the increase of the fluid within the volume.

2.1.3. Equation: Navier-Stokes

Porous media are modelled through the addition of momentum source in terms of the governing equation of fluid flow. The sink term presented as equations (4) and (6) is assembled of two parts, of which Darcy law represents the left part and the right part considers the force of inertia.

and are the source term for the *i-th* (x, z) directions in the momentum equations (4) and (6).

X-momentum:

$$\rho u \frac{\partial u}{\partial x} + \rho w \frac{\partial u}{\partial z} = -\frac{\partial p}{\partial x} + \mu\left(\frac{\partial^2 u}{\partial x^2} + \frac{\partial^2 u}{\partial z^2}\right) + S_x \tag{3}$$

$$S_x = -\left(\frac{\mu}{\alpha}u + C_2 \frac{1}{2}\rho |u| u\right) \tag{4}$$

Z-momentum:

$$\rho u\frac{\partial w}{\partial x}+\rho w\frac{\partial w}{\partial z}=-\frac{\partial p}{\partial z}+\mu\left(\frac{\partial^2 w}{\partial x^2}+\frac{\partial^2 w}{\partial z^2}\right)+S_z \tag{5}$$

$$S_z=-\left(\frac{\mu}{\alpha}w+C_2\frac{1}{2}\rho|w|w\right) \tag{6}$$

where α is the permeability and C_2 is the inertial resistance factor.

2.2. Boundary Conditions

- No slip conditions on the walls: ($u = w = 0$);
- Inlet flow:

$$0\le x\le l\ \&\ z=(H-h):\begin{cases}w_z=w_{\text{int}}=1.74\times10^{-5}\\P_z=P_a+\rho gh\end{cases} \tag{7}$$

- Outlet flow:

$$x=L\ \&\ 0\le z\le e:\ \phi=\phi_{out}=e\cdot y\cdot w_{\text{int}}$$

- Symmetry conditions:

$$x=0\ \&\ 0\le z\le(H-h):\left(\frac{\partial u}{\partial z}\right)_{x=0}=0$$

$$x=L\ \&\ 0\le z\le(H-e):\left(\frac{\partial u}{\partial z}\right)_{x=l}=0$$

- Impermeable surfaces:

$$0\le x\le L\ \&\ z=0:\ w_{wall}=w_{fluid}=0$$

$$(L-l)\le x\le L\ \&\ z=H:\ w_{wall}=w_{fluid}=0$$

The transport equations (2) (3) and (5) are resolved by the control volume method and solved by the SIMPLE algorithm [15]–[16], according to the first order-implicit numerical scheme. The equations of the algebraic system obtained have been solved by the Gauss–Seidel iterative method. It is estimated that the conver-

gence is reached when the relative differences of all the calculated variables, at the different nodes of the mesh, become less than 10^{-5} between two successive iterations.

2.3. The Validity of Darcy Law

The balance between viscous and inertial forces are expressed by a non-dimensional parameter called the Reynolds number:

$$R_e = \frac{\rho v d}{\mu} \tag{8}$$

where R_e is Reynolds number, ρ is fluid density, v is fluid velocity, d is the diameter of the passageway through which the fluid moves, μ is dynamic fluid viscosity.

The authors of the present research have proven theoretically by solving the Navier–Stokes equations in the case $R_e << 1$ (that is, when the inertial terms are negligible). The authors see that the Navier–Stokes equations are called "Stokes equations"; this relationship is called the Stokes law and it is useful, for example, for calculating a sedimentation rate of fine particles (it is necessary that $R_e << 1$).

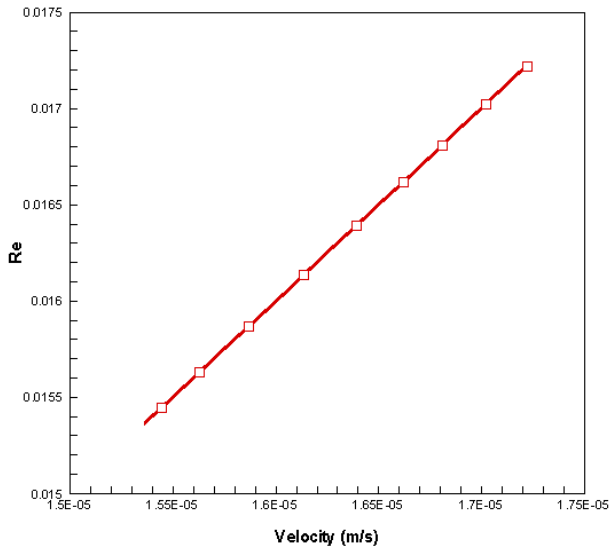

Fig. 2. The validity of Darcy's law (Re vs. Velocity).

At high Reynolds numbers, the relationship between specific discharge and hydraulic gradient is no longer linear. Therefore, the transition zone of Reynolds numbers in the range of 1–10 is associated with the upper limit of Darcy's law [17]. Such circumstances may occur in fracture flow and adjacent to wells that are pumping at high rates.

The lower limit of Darcy law (8) is associated with extremely slow groundwater movement. In such cases, other gradients, such as thermal, chemical and/or

electrical, may be stronger than the hydraulic gradient and may control the movement of flow.

The results shown in Fig. 2 demonstrate that regardless of the values taken by the pressure drop and the filtration rate the number of Re always remains less than 1. Thus, the criterion of Darcy is systematically validated in the studied cases.

2.4. Stationary Value for Pressure

The evolution of the pressure of the groundwater flow in the vertical plane and in the middle of the aquifer studied (reference zone), represented in Fig. 3, comprises two successive phases, i.e., the transitional phase between the first iteration and the 10th iteration, which depends strongly on the initial state of the system, and the phase of established regime, or thence of the latter, independent of the initial state of the system (initial conditions).

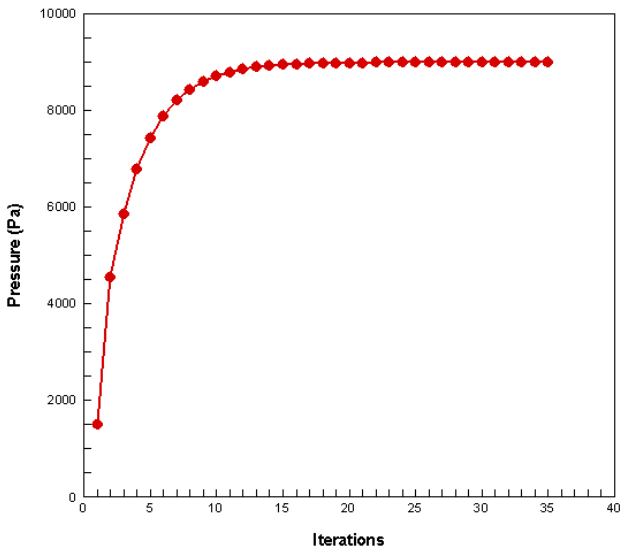

Fig. 3. Stationary value for pressure (particular setup).

2.5. Test Meshes

For a gradually varied flow, it takes large longitudinal distances to observe significant changes in height; in areas where the flow rapidly varied, the meter is an acceptable longitudinal length scale. As the simulation is carried out over a distance of 100m of languor and 50m of depth, one can expect a realistic solution, placing a calculation node every meter. Then coarse meshes have been selected.

Thus, choosing a fine mesh, there is a clear solution of what the authors are willing to achieve. Conversely, for a coarse mesh, the authors have an estimate of the solution. The authors do not know how in practice an interpolation is done, but they believe that it is made without regard to the physical solution between two nodes.

The authors have calculated the residual values for each solution. Residues have been found in the same order of magnitude as the authors expected to have large residuals for coarse meshes.

Table 1

Test Meshes

Cases	Mesh	Nodes	u_{max} *(m/s)*	w_{max} *(m/s)*	Velocity magnitude (m/s)	Error (%)
1	5 (m)x5(m)	223	0.027	0.0033	0.030	2.33
2	2.5(m) x 2.5(m)	829	0.037	0.0083	0.044	1.98
3	1.5(m) x 1.5(m)	1276	0.030	0.0080	0.037	-

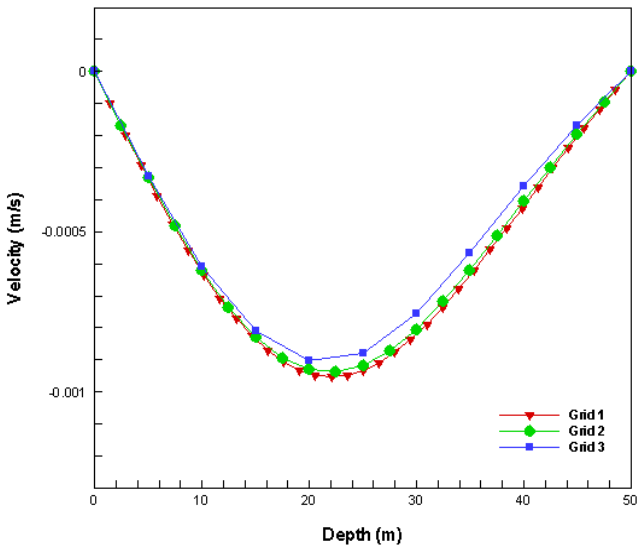

Fig. 4. Test meshes: (Velocity vs. Depth).

To sum up, if the number of nodes is increased, the number of errors is reduced due to interpolation between the nodes, and the numerical solution is closer to reality. It has also been noted that the computation time increases with the fineness of the mesh, but this increase (Error < 2.33 %) is not significant for the meshes chosen in the present simulations.

3. INTERPRETATION OF RESULTS

3.1. Pressure Drop vs. Velocity

The variation of clean pressure drop with the velocity is given in Fig. 5.

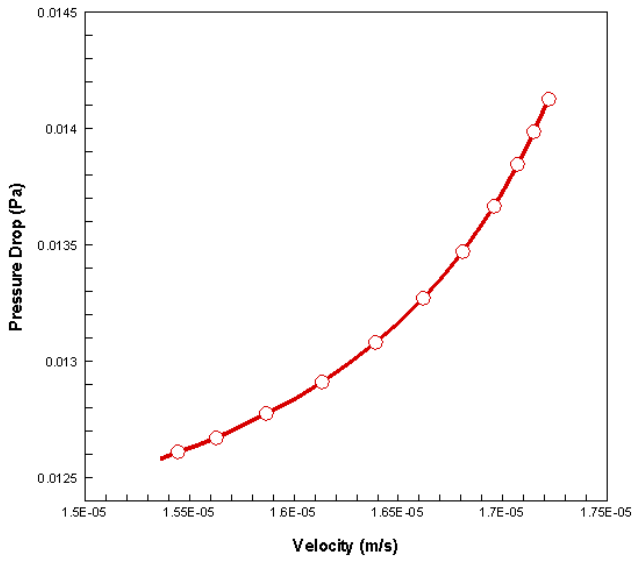

Fig. 5. Evolution of pressure vs. velocity.

It can be observed from Fig. 5 that pressure drop for clean water increases with increased inflow rate (feed rate). When the inlet feed rate increases, the tangential velocity of flow in the aquifer increases. Thereby the centrifugal force on water molecules increases and gives high velocity. It has been found that the clean pressure drop varies 1.44 to the power of velocity as shown in equation 9.

$$\Delta p = 0.4886 \cdot w^{1.4397} \tag{9}$$

where – clean pressure drop, P_a, and w – velocity, (m/s).

3.2. Streamlines and Velocity Field

It is observed in Fig. 6 that the flow of water into the aquifer moves in layers, which glide one over the other, without mixing, and the flow is laminar. The current streamlines traced in the fluid whose tangents at all points are parallel to the direction of flow and are generally curved but never intersect.

The flow is a flat flow, in a vertical direction from the river to the aquifer, on the one hand, and horizontal from the aquifer to the storage basin, on the other.

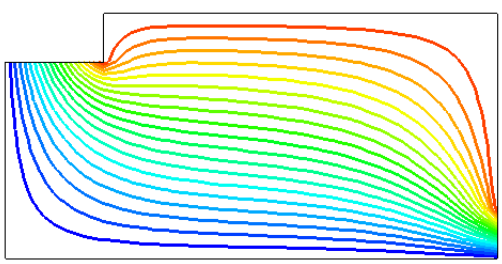

Fig. 6. Streamlines and velocity field.

The velocity field demonstrated in Fig. 7 shows that the velocity is zero close to the impermeable walls due to the non-slip condition, the maximum values are observed at the level of water infiltration from the river to the aquifer and at the level of the aquifer towards the storage area.

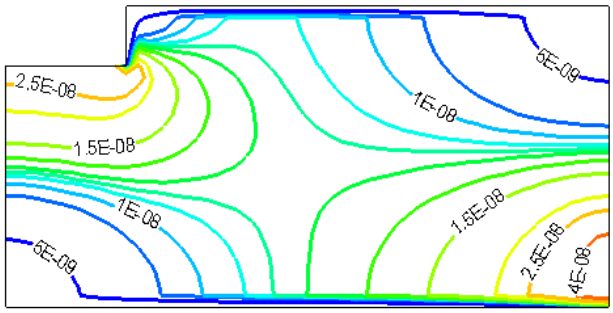

Fig. 7. Streamlines and velocity field.

3.3. Pressure Drop Field

It is seen that the flows are organised according to the search for the most advantageous outlets (Fig. 8) (evacuation of a maximum of flows with a minimum of losses of load). The observation of the load change in approaching the watercourse banks to identify what situation you are in. Thus, increasing loads towards the river show a river-slick flow.

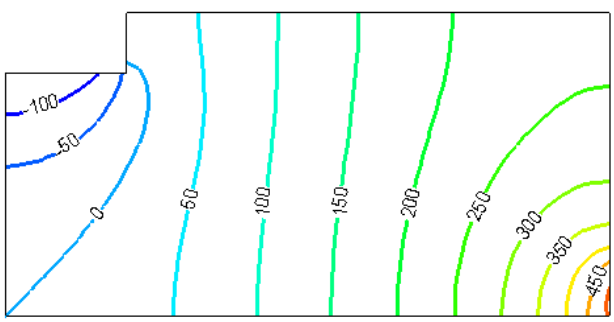

Fig. 8. Pressure drop field.

The piezometric lines are doubly influenced by:

- the general direction of flow of the water table (in accordance with the flow direction of the river in the general case).
- relations with the river, depending on whether it is supported by the groundwater or fed by the water table (a situation that can be reversed depending on the season and / or the intensity of the anthropogenic withdrawals in the groundwater).

4. CONCLUSIONS

This approach presents a coupling between the Darcy–Forchheimer equations and the mass and momentum conservation equations (Navier–Stokes) to describe these interactions (river / aquifer) on a local scale. The flow of water into the soil varies according to the multiplicity of paths taken by the drops of water. The interaction between rivers and aquifers describes the main phenomenon of infiltration (passage of water across the soil surface under the effect of gravity) that constitutes the path of groundwater. The flow of infiltrating water varies according to the influence of several physical and geological factors. These include percolation (flow of liquid in unsaturated soil due to gravity) and capillary rise (ascent of water above the underground water table by capillarity). The behaviour of these two phenomena is dependent on the properties of aquifers, especially hydraulic conductivity, as demonstrated by the Darcy experiment, which is the basis for the modelling of underground flows.

REFERENCES

1. Beavers, G.S., & Joseph, D.D. (1967). Boundary conditions at naturally permeable wall. *Journal of Fluid Mechanics*, *30*(1), 197–207.
2. Saffman, P.G. (1971). On the boundary condition at the surface of a porous medium. *Studies in Applied Mathematics, 50*(2), 93–101.
3. Correa, M.R., & Loula, A.F.D. (2009). A unified mixed formulation naturally coupling Stokes and Darcy flows. *Computer Methods in Applied Mechanics and Engineering*, *198*(33-36), 2710–2722.
4. Urquiza, J.M., N'Dri, D., Garon A., & Delfour, M.C. (2008). Coupling Stokes and Darcy equations. *Applied Numerical Mathematics*, *58*(5), 525–538.
5. Pacquaut, G., Bruchon, J., Moulin N., & Drapier, S. (2011). Combining a level-set method and a mixed stabilized P1/P1 formulation for coupling Stokes-Darcy flows. *International Journal for Numerical Methods in Fluids*, *66*.
6. Gatica, G.N., Oyarzúa, R., & Sayas, F.-J. (2011). Convergence of a family of Galerkin discretizations for the Stokes-Darcy coupled problem. *Numerical Methods for Partial Differential Equations*, *27*(3), 721–748.
7. Masud, A. (2007). A stabilized mixed finite element method for Darcy-Stokes flow. *International Journal for Numerical Methods in Fluids*, *54*(6–8), 665–681.
8. Tan, H., & Pillai, K. M. (2009). Finite element implementation of stress-jump and stress-continuity conditions at porous-medium, clear-fluid interface. *Computers & Fluids*, *38*(6), 1118–1131.
9. Arquis, E., & Caltagirone, J.P. (1984). Sur les conditions hydrodynamiques au voisinage d'une interface milieu _uide-milieu poreux : application à la convection naturelle. *Comptes Rendus de l'Académie des Science de Paris, Série II*, *299*, 1–4.
10. Arquis, E., Caltagirone, J.P., & Le Breton, P. (1991). Détermination des propriétés de dispersion d'un milieu périodique à partir de l'analyse locale des transferts thermiques. *Comptes Rendus de l'Académie des Science de Paris, Série II*, *313*, 1087–1092.
11. Vincent, S., Caltagirone, J.-P., Lubin, P., & Randrianarivelo, T.-N. (2004). An adaptative augmented lagrangian method for three-dimensional multimaterial flows. *Computers & Fluids*, *33*, 1273–1289.

12. Randrianarivelo, T.N., Pianet, G., Vincent S., & Caltagirone, J.-P. (2005). Numerical modelling of solid particle motion using a new penalty method. *International Journal for Numerical Methods in Fluids*, *47*, 1245–1251.
13. Sarthou, A., Vincent, S., Caltagirone, J.-P., & Angot, P. (2008). Eulerian lagrangian grid coupling and penalty methods for the simulation of multiphase flows interacting with complex objects. *International Journal for Numerical Methods in Fluids*, *56,* 1093–1099.
14. Puaux, G. (2011). Numerical simulation of flows at microscopic and mesoscopic scales in RTM process. PhD thesis. *École nationale supérieure des mines de Paris*.
15. Patankar, S.V. (1980). Numerical Heat Transfer and Fluid Flow. Hémisphère Inc.: McGraw-Hill, Washington, États-Unis.
16. Versteeg, H.K, & Malalasekera, W. (1995). Introduction to Computational Fluid Dynamics: The Finite Volume Method. Wiley, New York, États-Unis.
17. Bear, J. (1972). Dynamics of fluids in porous media. Elsevier.

SKAITLISKĀ PIEEJA ŪDENS PLŪSMAS RAKSTUROŠANAI NEPIESĀTINĀTAJĀ PORAINĀ VIDĒ, APVIENOJOT NAVJĒ-STOKSA UN DARSĪ-FORHEIMERA VIENĀDOJUMUS

K. Hami, I. Zeroual

K o p s a v i l k u m s

Šajā pētījumā tika veiktas simulācijas, lai skaitliski noteiktu upes barotās pazemes ūdens plūsmas dinamiskos raksturlielumus. Pamata vienādojumi, kas regulē pētāmo problēmu, ir kustības daudzuma saglabāšanās jeb Navjē-Stoksa vienādojumi (plūsma starp porām), kurus apvieno ar Darsī-Forheimera vienādojumiem (plūsma šajās porās). Lai izprastu iesaistītās parādības, autori vispirms pēta plūsmas ātruma ietekmi uz spiedienu un filtrēšanas ātrumu pazemes vidē, pēc tam aprēķina upes ūdens līmeņa paaugstināšanās ietekmi uz plūsmas uzvedību ūdens nesējslāņa piesātinātajā un nepiesātinātajā daļā.

20.02.2017.

LATVIAN JOURNAL OF PHYSICS AND TECHNICAL SCIENCES
2017, N 6

DOI: 10.1515/lpts-2017-0042

ELECTRONICS

COMPARISON OF CHROMATIC DISPERSION COMPENSATION METHOD EFFICIENCY FOR 10 GBIT/S RZ-OOK AND NRZ-OOK WDM-PON TRANSMISSION SYSTEMS

A. Alsevska, V. Dilendorfs, S. Spolitis, Vj. Bobrovs
Institute of Telecommunications, Riga Technical University,
12 Azenes Str., Riga, LV-1048, LATVIA
E-mail: Valts.Dilendorfs@rtu.lv

In the paper, the authors compare efficiency of two physical dispersion compensation methods for single channel and 8-channel WDM fibre-optical transmission systems using return-to-zero (RZ) and non-return-to-zero (NRZ) line codes for operation within optical C-band frequencies by means of computer simulations. As one of the most important destructive effects in fibre optical transmission systems (FOTS) is chromatic dispersion (CD), it is very important to reduce its negative effect on a transmitted signal. Dispersion compensation methods that were implemented in the research were dispersion compensating fibre (DCF) and fibre Bragg grating (FBG). The main goal of the paper was to find out which dispersion compensation method (DCF or FBG) provided the highest performance increase for fibre-optical transmission system and provided the longest transmission distance after dispersion compensation was implemented at different locations in the fibre-optical line while RZ or NRZ line codes were used. In the paper the reference point of signal quality for all measurements, which were obtained at the receiver, was BER<10^{-12}.

Keywords: *DCF, DCM, dispersion, dispersion compensation, FBG, optical access, optical fibre, SMF, WDM-PON*

1. INTRODUCTION

The development of telecommunication systems in the near future is focused on the increasing data transmission speeds for all kinds of electronic devices, especially wireless devices. Mobile network operators are still heavily interested in improving mobile network from 3G to 4G, 4G+ and preparing for 5G. While transmission speeds and service coverage areas increase, wireless network operators are still unable to provide sufficient transmission speed and quality as fibre-optical connection can. There are a number of compelling advantages for using fibre-optics, for example, fibre-optic cabling provides a much higher bandwidth, fibre-optics do not suffer from intersymbol interference and have much lower levels of signal attenuation [1].

One solution for efficient utilisation of fibre optical network in urban areas without the need for installing additional optical fibres to backbone network is adopting dense wavelength division multiplexing (DWDM) transmission systems. DWDM is a transmission system that enables more efficient utilisation of optical fibre by multiplexing and simultaneously transmitting multiple optical signals of different wavelengths [2]. Even though the fibre optical transmission systems (FOTS) are the backbone of all worlds' communications, system itself has undesirable effects which are necessary to prevent or reduce. The most common destructive effect for FOTS is chromatic dispersion (CD). CD is the term given to the phenomenon by which different spectral components of a pulse travel at different velocities. The negative effect of CD in FOTS increases with the increase of bit rate or optical fibres length. When one or both conditions are fulfilled the effect of CD must be taken into consideration but if it is ignored, dispersion can completely corrupt transmitted data because of intersymbol interference (ISI) [3].

There are many methods how to compensate CD, but two the most popular methods are dispersion shifted fibre (DCF) and fibre Bragg grating (FBG) [3]– [4]. DCF and FBG detailed explanation are written in the second section.

When higher bit rates such as 10 Gbit/s and above and/or high transmitted powers are transmitted, it is important to consider the influence of nonlinear optical effects (NOE). In the case of WDM systems, nonlinear effects can become important even at moderate powers and bit rates. NOE are often categorised into two categories of nonlinear effects. The first arises due to the interaction of light waves with phonons in the silica medium. The main effects in this category are stimulated Brillouin scattering (SBS) and stimulated Raman scattering (SRS). The second set of nonlinear effects arises due to dependence of the refractive index on the intensity of the applied electric field. The most important NOE in this category are self-phase modulation (SPM) and four wave mixing (FWM) [3]. Single-channel nonlinear effects manifest mainly through self-phase modulation (SPM), whereby each channel alters its own phase. SPM translates into pulse distortions through chromatic dispersion [3], [5]. WDM nonlinear effects are often split into cross phase modulation (XPM), whereby the phase of each channel is modified by the power of the neighbouring channels, and four wave mixing (FWM), whereby three channels interact to transfer a fraction of their energy to a fourth one [3], [6]. Due to previously mentioned destructive influence on FOTS performance, the maximal transmission line length, with 10 Gbit/s transmission speed, is less than 100 km [7].

Within the framework of the research, non-return-to-zero (NRZ) and return-to-zero (RZ), the most common on-off keying (OOK) signal line codes, were studied. The most common line code – NRZ for 1 bit representation occupies the entire bit interval at constant power level. RZ is another common line code which occupies only a fraction of the bit interval that depends on a duty cycle. Typical duty cycle is 50 %. If NRZ and RZ line code bandwidths are compared, then it is possible to determine that RZ line code occupies about half larger bandwidth than NRZ line code and this is also the main difference between NRZ and RZ [8]. RZ line code has also greater tolerance to nonlinear effects like – SPM, XPM and FWM. On the one hand, the NRZ line code is more suitable for WDM systems; on the other hand, the RZ line code is found to be less susceptible to inter-symbol interference (ISI) due to

a smaller impact of NOE and so typically achieves better performance compared to NRZ [9].

The main purpose of this paper is to investigate the most popular dispersion compensation methods – DCF and FBG for dispersion compensation efficiency using RZ and NRZ line codes for single- and 8-channel transmission systems with 10 Gbit/s transmission speed.

In the beginning, simulations of dispersion compensation are executed for a single channel system, but then simulations are repeated for 8- channel WDM FOTS with 100 GHz channel spacing. The paper shows how fibre-optical transmission systems with RZ or NRZ line code are affected by different dispersion compensation methods and also how dispersion compensation location in a fibre-optical transmission line influences the length of fibre-optical transmission lines.

2. DISPERSION COMPENSATION METHODS

Dispersion is the name given to any effect wherein different components of the transmitted signal travel at different velocities in the fibre, arriving at different times at the receiver. A signal pulse launched into a fibre arrives smeared at the other end as a consequence of this effect. Dispersion is a cumulative effect – the longer the link, the greater the amount of dispersion. Standard single mode fibre (SMF) has a positive dispersion value of around 16 ps/(nm·km) at 1550 nm. The destructive impact of CD increases if FOTS transmissions speed is also increased, particularly for system with 10 Gbit/s bit rate or higher [7].

Dispersion management is a very important part of designing WDM transmission systems, since dispersion affects the penalties due to various types of fibre nonlinearities. There are several techniques to reduce the impact of CD – external modulation in conjunction with DFB lasers, use of fibre with small chromatic dispersion value, and chromatic dispersion compensation [2]. In the present paper, the main objective is to investigate chromatic dispersion compensation with DCF and FBG. The two most common methods can be used as dispersion-compensating module (DCM) for dispersion compensation purposes.

DCF is special fibre developed for CD compensation. DCF has a negative dispersion value of around -80 ps/(nm·km) (SMF has a positive value of 16 ps/(nm·km)) at 1550 nm and core effective area of 20 μm^2 (compared to SMF 85 μm$^{2)}$. The required amount of dispersion compensation can be calculated by the following equation (1).

$$D(\lambda_{\mathrm{SMF}})L_{SMF} + D(\lambda_{DCF})L_{DCF} = 0 \tag{1}$$

In equation (1) variables $D(\lambda_{SMF})$ and $D(\lambda_{DCF})$ are dispersion coefficients ps/(nm·km) for single-mode fibre (SMF) and dispersion compensating fibre (DCF) at certain wavelength (λ, nm), but L_{SMF} and are the lengths of fibres (in km). It is important not to reduce CD value to zero because of FWM increases due to the genera-

tion of new beat frequencies [10]. Because of wide performance bandwidth, stable performance and minimal temperature dependence, DCF have become one of the most used method for CD compensation. One DCF disadvantage is its large added loss to the system – 0.55 dB/km.

Part of the fibre where period of the refractive index grating varies along the length of the fibre is called chirped fibre Bragg grating (FBG). When FOTS optical signal propagates through chirped fibre Bragg grating, different wavelength components will get reflected at different positions along the grating. As transmitted optical signal contains different wavelength components and these optical signal components will be reflected, depending on the wavelength, at different positions along the grating, it is possible to use this ability to compensate CD. Dispersion compensation using FBG has some advantages over DCF, for example, FBG is smaller in size physically, exhibits relatively small insertion loss and causes negligible nonlinearities [4]. FBG ideally is suited for individual wavelength compensation rather than multiple wavelengths, but, in contrast, DCF is better suited for compensation over a wide range of wavelengths.

The physical location of optical components inside FOTS can also impact the performance of FOTS. Because of this property, DCM (DCF or FBG) can be placed at three different locations in the transmission system for CD pre-compensation, post-compensation and symmetrical compensation.

3. EXPERIMENTAL SIMULATION MODEL

For experimental simulation, *RSoft* simulation program *OptSim* was used. *OptSim* is widely used for design of high-performance optical communication systems. In the paper, single- and 8-channel WDM system mathematical modelling, with different on-off keying (OOK) modulation formats (RZ and NRZ), was shown, exploring how CD changed the performance of FOTS system when DCM units were implemented in the system.

In the simulation, transmission speed for single-channel and 8-channel systems was set to 10 Gbit/s per channel. Transmitter, for a single-channel system, was constructed from 4 elements – the data source, RZ or NRZ coder, continuous wave laser (CW) as a light source, Mach-Zehnder amplitude modulator. For an 8-channel system, additional optical Raised-Cosine filter was added with 60 GHz bandwidth at -3dB and 0.1 roll-off factor. For a single-channel system, two central frequencies of different channels were chosen - 193.1 THz and 195.9 THz. For 8-channel simulations, central frequencies were chosen starting from the 1st to the 8th channel, again two different frequency bandwidths were chosen and they ranged from 193.1 THz to 193.8 THz and from 195.9 THz to 196.6 THz. Channel frequencies were chosen according to ITU-T G.694.1 recommendation. Receiver, for all channels, was composed of 3 elements – the optical Raised-Cosine filter, PIN receiver diode and fifth order electrical Bessel filter with 8 GHz bandwidth at -3dB. Arrayed waveguide grating (AWG) multiplexer and demultiplexer were formed from optical power splitter and combiner together with optical filters [11]. A complete simulation model for an 8-channel WDM system is shown in Fig. 1 and the basic parameters of setup

components are shown in Table 1.

Simulation model and the basic parameters of components for a single-channel system remain the same if compared with an 8-channel system, the only difference is the removal of excess transmitters, receivers and coupler/splitter.

The main aim at first was to obtain maximum line length for both a single-channel system and an 8-channel WDM system without dispersion compensation. All simulations were executed for both RZ and NRZ line codes. We chose BER<10^{-12} as the reference threshold for all channels in our investigated transmission systems to determine the maximum line length. After maximum line length was clarified, all simulations were repeated only with one exception –additional DCM modules were added for CD compensation. DCM module consisted of one of the two most common dispersion compensation methods – DCF or FBG. In addition, DCM location was changed in FOTS with the aim of clarifying how the location of DCM would change the performance of individual channels in a single-channel system and an 8-channel WDM system.

At first, simulations were executed for a single-channel system with RZ line code using DCF as DCM in all possible combinations in FOTS. Afterwards, DCF was substituted with FBG and simulations were repeated. Then RZ line code was changed for NRZ line code and simulations for a single-channel system were repeated. The same steps were repeated with simulations of an 8-channel system. In total, 56 simulations were completed.

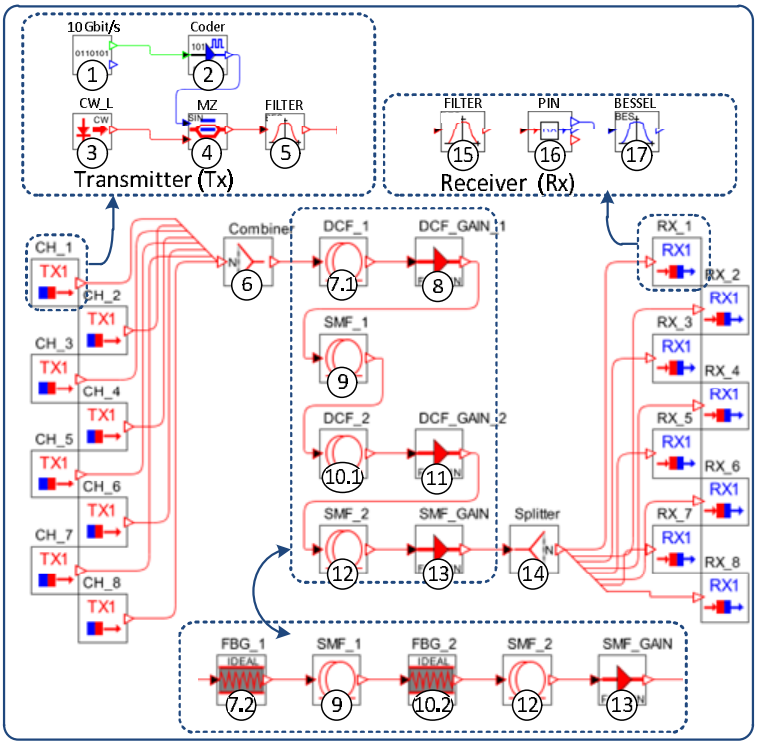

Fig. 1. Simulation model of 8-channel, 10 Gbit/s, optical fibre transmission system with symmetrical CD compensation for SMF.

Table 1

Basic Parameter Values for 8-Channel Simulation Model Components

No.	Components	Basic parameters (1 CHANNEL)	Basic parameters (8 CHANNELS)
1	Data source	Data rate: 10 Gbit/s	Data rate: 10 Gbit/s
2	Coder (RZ or NRZ)	RZ Duty cycle: 0.5	RZ Duty cycle: 0.5
3	CW laser	Output power: 3 dBm, FWHM linewidth: 1 MHz Central emission frequency: 193.1 THz or 195.9 THz	Output power: 3 dBm, FWHM linewidth: 1 MHz Channels central frequencies: 1st to 8th: 193.1 THz - 193.8 THz or 195.9 THz - 196.6 THz Channel spacing: 100 GHz
4	Mach-Zehnder (MZ) amplitude modulator	Excess loss: 3 dB	Excess loss: 3 dB
5	Optical Raised-Cosine filter	-	Roll-off factor: 0.1 -3dB bandwidth: 60 GHz
6	Optical combiner	-	Attenuation: 0 dB
7.1	DCF fiber Nr.1	Loss: 0.55 dB/km Dispersion: -80 ps/(nm·km) Core effective area: 20 μm^2	Loss: 0.55 dB/km Dispersion: -80 ps/(nm·km) Core effective area: 20 μm^2
7.2	FBG Nr.1	Variable dispersion value, ps/(nm·km)	Variable dispersion value, ps/(nm·km)
8	DCF Gain Nr.1 (EDFA optical amplifier)	Variable gain, dB	Variable gain, dB
9	SMF fiber Nr.1	Loss: 0.2 dB/km Dispersion: 16 ps/(nm·km) Core effective area: 80 μm^2	Loss: 0.2 dB/km Dispersion: 16 ps/(nm·km) Core effective area: 80 μm^2
10.1	DCF fiber Nr.2	Loss: 0.55 dB/km Dispersion: -80 ps/(nm·km) Core effective area: 20 μm^2	Loss: 0.55 dB/km Dispersion: -80 ps/(nm·km) Core effective area: 20 μm^2
10.2	FBG Nr.2	Variable dispersion value, ps/(nm·km)	Variable dispersion value, ps/(nm·km)
11	DCF Gain Nr.2 (EDFA optical amplifier)	Variable gain, dB	Variable gain, dB
12	SMF fiber Nr.2	Loss: 0.2 dB/km Dispersion: 16 ps/(nm·km) Core effective area: 80 μm^2	Loss: 0.2 dB/km Dispersion: 16 ps/(nm·km) Core effective area: 80 μm^2
13	Gain Nr.3	Gain: 10 dB	Gain: 10 dB
14	Splitter	-	Attenuation: 0 dB
15	Optical Raised-Cosine filter	-	Roll-off factor: 0.1 -3dB bandwidth: 60 GHz
16	Receiver	Photodiode: PIN Sensitivity: -23.9 dBm Error probability: 10^{-9}	Photodiode: PIN Sensitivity: -23.9 dBm Error probability: 10^{-9}
17	Electrical Bessel filter	Number of poles: 5 -3dB bandwidth: 8 GHz	Number of poles: 5 -3dB bandwidth: 8 GHz

4. RESULTS AND DISCUSSION

When RZ line code was used, the maximum transmission line length for a single-channel system without CD compensation at 193.1 THz was L=49.0 km (accumulated dispersion value 784.0 ps/nm, BER=$5.4 \cdot 10^{-13}$), but at 195.9 THz L=56.4 km (accumulated dispersions value 901.9 ps/nm, BER=$9.5 \cdot 10^{-13}$). While using NRZ line code, the maximum transmission line length for a single channel system without CD compensation at 193.1 THz was L=84.4 km (accumulated dispersion value 1350.4 ps/nm, BER=$6.2 \cdot 10^{-13}$), but at 195.9 THz L=92.1 km (accumulated dispersion value 1473.6 ps/nm, BER=$8.8 \cdot 10^{-13}$). Further activities for a single-channel system were to completely compensate CD using both DCF and FBG. When CD compensations were performed by DCF, an additional amplifier was used for DCF insertion loss compensation, but FBG insertion loss was set to 0 dB (in simulation FBG component). At first, CD compensation was executed for a single channel system with RZ line code, at both frequencies, using DCM for pre-compensation, post-compensation and symmetrical compensation, but then CD compensation was executed for a system with NRZ line code, for the both frequencies as well. A total of 6 different combinations were investigated for each line code formats and each frequency. All results for single-channel system simulations are demonstrated in Table 2.

Table 2

Maximal Provided Transmission Distances for Single-Channel Communication Systems with RZ and NRZ Line Codes

SINGLE-CHANNEL, RZ line code								
Frequency	**DC methods**	**Without DC**	**1. Pre- DC (DCF)**	**2. Post- DC (DCF)**	**3. Pre- and Post- DC (DCF)**	**4. Pre- DC (FBG)**	**5. Post- DC (FBG)**	**6. Pre- and Post- DC (FBG)**
193.1 THz	Max. line length, km	49.0	97.2	97.2	97.3	97.3	97.5	97.6
	Extension length, km		48.2	48.2	48.3	48.3	48.5	48.6
	Extension length, %	**-**	**49.6**	**49.6**	**49.7**	**49.7**	**49.7**	**49.8**
195.9 THz	Max. line length, km	56.4	117.1	116.8	115.6	116.5	115.8	115.5
	Extension length, km		60.7	60.4	59.2	60.2	59.5	59.2
	Extension length, %	**-**	**51.9**	**51.7**	**51.2**	**51.6**	**51.3**	**51.2**
SINGLE-CHANNEL, NRZ line code								
193.1 THz	Max. line length, km	84.4	157.8	157.6	157.7	155.7	156.8	156.9
	Extension length, km		73.4	73.2	73.3	71.3	72.4	72.5
	Extension length, %	**-**	**46.5**	**46.5**	**46.5**	**45.8**	**46.2**	**46.2**
195.9 THz	Max. line length, km	92.1	148.7	145.1	146.5	147.9	147.3	147.3
	Extension length, km		56.6	53.0	54.4	55.8	55.2	55.2
	Extension length, %	**-**	**38.1**	**36.5**	**37.1**	**37.7**	**37.5**	**37.5**

When RZ line code was used, the longest optical line for a single-channel system at 193.1 THz was L=97.6 km, which was achieved using FBG for dispersion

pre- and post-compensation, but at 195.9 THz the longest optical line was L=117.1 km, which was achieved using DCF for dispersion pre-compensation. When NRZ line code was used, the longest optical line for a single-channel system at 193.1 THz was L=157.8 km, but at 195.9 THz, L=148.7 km and the both results were achieved using DCF for dispersion pre-compensation.

For an 8-channel WDM system, the results were quite similar. All results for 8-channel system simulations are presented in Table 3. When RZ line code was used, the longest optical line using channel frequencies from 193.1 to 193.8 THz was L=98.6 km, but using 195.9–196.6 THz L=118.0 km, and the both results were achieved using DCF for dispersion pre-compensation. When NRZ line code was used, the longest optical line using channel frequencies from 193.1 to 193.8 THz was L=143.9 km and again this result was achieved using DCF for dispersion pre- compensation. However, using channel frequencies from 193.1 to 193.8 THz the longest optical line was L=144.3 km when FBG was used for dispersion post-compensation.

Table 3

Maximal Provided Transmission Distances for 8-Channel Communication Systems with RZ and NRZ Line Codes

8 CHANNELS, RZ line code								
Frequency	**DC methods**	**Without DC**	**1. Pre- DC (DCF)**	**2. Post- DC (DCF)**	**3. Pre- and Post- DC (DCF)**	**4. Pre- DC (FBG)**	**5. Post- DC (FBG)**	**6. Pre- and Post- DC (FBG)**
193.1-193.8 THz	Max. line length, km	49.7	98.6	98.5	98.5	98.5	97.9	98.0
	Extension length, km		48.9	48.8	48.8	48.8	48.2	48.3
	Extension length, %	**-**	**49.6**	**49.5**	**49.6**	**49.5**	**49.2**	**49.3**
195.9-196.6 THz	Max. line length, km	56.1	118.0	117.6	117.9	115.9	115.7	115.7
	Extension length, km		61.9	61.5	61.8	59.8	59.6	59.6
	Extension length, %	**-**	**52.5**	**52.3**	**52.4**	**51.6**	**51.5**	**51.5**
8 CHANNELS, NRZ line code								
193.1-193.8 THz	Max. line length, km	81.4	143.9	143.0	142.8	143.5	143.8	143.8
	Extension length, km		62.5	61.6	61.4	62.1	62.4	62.4
	Extension length, %	**-**	**43.4**	**43.1**	**43.0**	**43.3**	**43.4**	**43.4**
195.9-196.6 THz	Max. line length, km	92.0	143.5	141.7	141.6	143.0	144.3	142.7
	Extension length, km		51.5	49.7	49.6	51.0	52.3	50.7
	Extension length, %	**-**	**35.9**	**35.1**	**35.0**	**35.7**	**36.2**	**35.5**

Tables 2 and 3 demonstrate by how much it is possible to extend the optical line, after performing DC for SMF. By comparing the length of extension fibres with the total length of fibres, it is possible to see which frequencies are affected more by dispersion. On average, for single-channel systems using 193.1 THz channel central frequency, it was possible to extend optical line transmission length by 49.7 % (DCF – 49.6 %, FBG – 49.7 %) but using 195.9 THz by 51.5 % (DCF – 51.6 %, FBG – 51.4 %) when RZ line code was used. When NRZ line code was used, it was possible

to extend optical line transmission length by 46.3 % (DCF – 46.5 %, FBG – 46.1 %) using 193.1 THz, and by 37.4 % (DCF – 37.3 %, FBG – 37.6 %) using 195.9 THz.

From these results it was concluded that using 193.1 THz, optical fibre line extension would be by 1.8 % shorter compared when 195.9 THz was used with RZ line code. A completely opposite situation was observed when NRZ line code was used. Using 193.1 THz, optical fibre line extension was by 8.9 % longer compared when 195.9 THz was used.

For an 8-channel WDM system, a similar pattern was observed compared to a single-channel system. Using channel central frequencies from 193.1 to 193.8 THz with RZ line code, the average line extension was 49.5 % (DCF – 49.6 %, FBG – 49.4 %), but using channel central frequencies from 195.9 to 196.6 THz the average line extension was 52.0 % (DCF – 52.4 %, FBG – 51.5 %). However, when NRZ line code was used, the average line extension was 43.3 % (DCF – 43.2 %, FBG – 43.4 %) and 35.6 % (DCF – 35.3 %, FBG – 35.8 %), respectively.

From these results it was concluded that using channel central frequencies from 193.1 to 193.8 THz, optical fibre line extension would be 2.5 % shorter compared when 195.9 to 196.6 THz was used with RZ line code. A completely opposite situation was observed when NRZ line code was used. When using channel central frequencies from 193.1 to 193.8 THz, optical fibre line extension was 7.7 % longer compared when 195.9 to 196.6 THz was used.

5. CONCLUSIONS

By using the investigated dispersion compensation methods, namely DCF and FBG, it was possible to compensate chromatic dispersion for single-channel and 8-channel optical WDM-PON transmission systems. On the basis of the obtained measurements for each simulated transmission system, the one dominant dispersion compensation method was observed. For single-channel systems where RZ and NRZ line codes were used for transmission on 193.1 THz and 195.9 THz central frequencies, the longest optical fibre transmission distances were reached when DCF was used for dispersion pre-compensation. However, with one exception –when RZ line code was used on 193.1 THz, the longest optical fibre transmission distance was reached with FBG dispersion pre- and post-compensation method. Nevertheless, for single-channel WDM-PON systems it would be advisable to use dispersion pre-compensation with DCF to obtain maximal system performance.

Dispersion compensation by using DCF for pre-compensation in 8-channel systems also gave the longest optical fibre transmission distance in most simulation models. When RZ line code is used for the both channel frequency ranges, dispersion pre-compensation with DCF is advisable. However, when NRZ line code was used, dispersion pre-compensation with DCF gave the longest optical fibre transmission distance if channel central frequencies were set from 193.1 to 193.8 THz with 100 GHz channel spacing. When channel central frequencies were set from 195.9 THz to 196.6 THz, with the same channel spacing, then dispersion post-compensation with FBG gave the best result. It would be advisable to avoid dispersion post-compensation with FBG when 193.1-193.8 THz frequency range is used and

pre- and post-compensation with DCF when 195.9-196.6 THz frequency range is used. In general, by using RZ line code it is possible to increase the total distance of optical fibre transmission lines by additional 3.4 % for 193.1 THz transmission frequency, comparing it with NRZ line code, but for 195.9 THz even by 14.1 %. For an 8-channel system, this correlation remains valid – the usage of RZ line code will increase the total distance of optical fibre transmission by 6.2 % when channel central frequencies are set from 193.1 THz to 193.8 THz comparing with NRZ line code, but for channel central frequencies from 195.9 THz to 196.6 THz the total distance of optical fibre transmission will increase even by 16.4 %.

While it is possible to determine the best results from each individual transmission frequency range, generally using both dispersion compensation methods and DCM locations, it is possible to obtain similar results, but the recommended dispersion compensation method for single-channel and 8-channel transmission systems is DCF, especially, when it is used as a dispersion pre-compensation solution.

REFERENCES

1. Senior, M.J., & Jamro, Y.M. (2009). *Optical fibre communications principles and practice.* Harlow, UK: Pearson Education Limited.
2. Chomycz, B. (2009). *Planning fibre optic networks*. USA: The McGraw-Hill Companies.
3. Ramaswami, K.R., Sivarajan, H., & Sasaki, H.G. (2010). *Optical Networks* (3rd Edition). Burlington, UK: Elsevier.
4. Kashyap, R. (2010). *Fibre Bragg gratings.* London, UK: Elsevier.
5. Ajmani, M., & Preeti, S.H. (2015). FWM in WDM system, effects and techniques to minimize: A review. In Fifth International Conference on Advanced Computing & Communication Technologies, 21–22 February 2015 (pp. 385–389). Haryana, India: IEEE.
6. Bhusari, S.N., Deshmukh, V.U., & Jagdale, S.S. (2016). Analysis of self-phase modulation and four-wave. In 2016 International Conference on Automatic Control and Dynamic Optimization Techniques (ICACDOT), 9–10 September 2016 (pp. 798–803). Pune, India: IEEE.
7. Kaminow, I.P., Li, T., & Willner, A.E. (2008). *Optical Fibre Telecommunications VB*, Burlington, UK: Elsevier.
8. Frenzel, L.E. (2015). *Handbook of serial communications interfaces*. Kidlington, UK: Newnes.
9. Bobrovs, V., Porins, J., & Ivanovs, G. (2007). Influence of nonlinear optical effects on the NRZ and RZ modulation signals in WDM systems. *Electronics and Electrical Engineering*, *4*(76), 55–58. ISSN 1392-1215.
10. Singh, M. (2015). Analyzing the effect of channel spacing and chromatic dispersion coefficient on FWM in optical WDM system. *International Journal of Signal Processing*, *8*(11), 99–110. ISSN: 2005-4254 IJSIP.
11. Spolitis, S., Bobrovs, V., & Ivanovs, G. (2012). Investigation of high-speed AWG filtered spectrum-sliced WDM PON system. In 8th International Symposium on Communication Systems, Networks and Digital Signal Processing (CSNDSP), 18–20 July 2012. DOI: 10.1109/CSNDSP.2012.6292658. Poznan, Poland: IEEE.

DISPERSIJAS KOMPENSĀCIJAS METOŽU EFEKTIVITĀTES SALĪDZINĀJUMS 10 GBIT/S RZ-OOK UN NRZ-OOK WDM-PON PĀRRAIDES SISTĒMĀM

A. Alševska, V. Dilendorfs, S. Spolītis, Vj. Bobrovs

K o p s a v i l k u m s

Optisko šķiedru izmantošanai pārraižu sistēmās ir vairākas priekšrocības, piemēram, optisko šķiedru kabeļi izmantošana nodrošināt lielāku signālu joslas platumu, optiskais signāls necieš no citu signālu elektromagnētiskajiem traucējumiem un signāla vājinājums optiskajā šķiedrā ir mazāks nekā jebkurā citā pārraides vidē. Blīvuma viļņgarumdales blīvēšana (DWDM) ir metode optisko pārraižu sistēmu veiktspējas palielināšanai, izmantojot optisko šķiedru efektīvāk - multipleksējot un vienlaikus pārraidot vairākus optiskos signālus ar dažādiem viļņu garumiem optiskajā šķiedrā. Šajā rakstā autori salīdzina divu dispersijas kompensāciju metožu efektivitāti, vienkanāla un 8-kanālu, DWDM optisko šķiedru pārraides sistēmām, izmantojot RZ un NRZ modulācijas formātus. Dispersijas kompensācija tiek realizētā izmantojot dispersiju kompensējošu šķiedru (DCF) un šķiedru Brega režģi (FBG). Šī raksta galvenais mērķis ir noskaidrot dispersijas kompensācijas metodi - DCF vai FBG, kura nodrošina vislielāko šķiedru optiskās pārraides sistēmas veiktspējas pieaugumu un spēj vienlaikus nodrošināt visgarāko pārraides attālumu pēc dispersijas kompensācijas. Izmantojot abas pētītās dispersijas kompensācijas metodes, pilnībā bija iespējams kompensēt hromatisko dispersiju vienkanāla un 8-kanālu DWDM optiskajās pārraides sistēmās.

12.11.2017.

LATVIAN JOURNAL OF PHYSICS AND TECHNICAL SCIENCES
2017, N 6

INDEX OF PAPERS PUBLISHED IN 2017

PHYSICAL AND TECHNICAL ENERGY PROBLEMS

SOLID STATE PHYSICS

PHYSICS

APPLIED PHYSICS

LATVIAN JOURNAL OF PHYSICS AND TECHNICAL SCIENCES
2017, N 6

2017. GADĀ PUBLICĒTO RAKSTU RĀDĪTĀJS

ENERĢĒTIKAS FIZIKĀLĀS UN TEHNISKĀS PROBLĒMAS

LATVIAN JOURNAL OF PHYSICS AND TECHNICAL SCIENCES
2017, N 6

УКАЗАТЕЛЬ СТАТЕЙ, ОПУБЛИКОВАННЫХ В 2017 ГОДУ

ФИЗИКО-ТЕХНИЧЕСКИЕ ПРОБЛЕМЫ ЭНЕРГЕТИКИ

ФИЗИКА ТВЕРДОГО ТЕЛА

ФИЗИКА